Quantifying and relating land-surface and subsurface variability in permafrost environments using LiDAR and surface geophysical datasets

S. S. Hubbard · C. Gangodagamage · B. Dafflon · H. Wainwright · J. Peterson · A. Gusmeroli · C. Ulrich · Y. Wu · C. Wilson · J. Rowland · C. Tweedie · S. D. Wullschleger

Abstract The value of remote sensing and surface geophysical data for characterizing the spatial variability and relationships between land-surface and subsurface properties was explored in an Alaska (USA) coastal plain ecosystem. At this site, a nested suite of measurements was collected within a region where the land surface was dominated by polygons, including: LiDAR data; ground-penetrating radar, electromagnetic, and electrical-resistance tomography data; active-layer depth, soil temperature, soil-moisture content, soil texture, soil carbon and nitrogen content; and pore-fluid cations. LiDAR data were used to extract geomorphic metrics, which potentially indicate drainage potential. Geophysical data were used to characterize active-layer depth, soil-moisture content, and permafrost variability. Cluster analysis of the LiDAR and geophysical attributes revealed the presence of three spatial zones, which had unique distributions of geomorphic, hydrological, thermal, and geochemical properties. The correspondence between the LiDAR-based geomorphic zonation and the geophysics-based active-layer and permafrost zonation highlights the significant linkage between these ecosystem compartments. This study suggests the potential of combining LiDAR and surface geophysical measurements for providing high-resolution information about land-surface and subsurface properties as well as their spatial variations and linkages, all of which are important for quantifying terrestrial-ecosystem evolution and feedbacks to climate.

Keywords Geomorphology · Geophysical characterization · Alaska · Active layer · Permafrost

Received: 26 May 2012 / Accepted: 15 November 2012

© Springer-Verlag Berlin Heidelberg (outside the USA) 2012

Published in the theme issue "Hydrogeology of Cold Regions"

S. S. Hubbard (✉) · B. Dafflon · H. Wainwright · J. Peterson · C. Ulrich · Y. Wu
Earth Sciences Division, Lawrence Berkeley National Laboratory, Berkeley, CA, USA
e-mail: sshubbard@lbl.gov
Tel.: +1-510-4865266

C. Gangodagamage · C. Wilson · J. Rowland
Los Alamos National Laboratory, Los Alamos, NM, USA

A. Gusmeroli
International Arctic Research Center, University of Alaska Fairbanks, Fairbanks, AK, USA

C. Tweedie
University of Texas at El Paso, El Paso, TX, USA

S. D. Wullschleger
Environmental Sciences Division, Oak Ridge National Laboratory, Oak Ridge, TN, USA

Introduction

The utility of surface geophysical and LiDAR (light detection and ranging) data, collected in an Arctic coastal tundra ecosystem, was examined to characterize the spatial variability and relationships between land-surface and subsurface properties that may influence terrestrial-ecosystem feedbacks to climate. The Arctic, characterized by the presence of permafrost, is a climatically sensitive region that has experienced warming in recent decades and that is projected to warm twice as much as the rest of the globe by the end of the twenty-first century (Allison et al. 2009). Permafrost soils store almost as much organic carbon as is found in the rest of the world's soils and about twice as much as is present in the atmosphere (Tarnocai et al. 2009); 12 % of that organic carbon is currently contained within the upper active layer with the remainder present in the vulnerable permafrost. Recent observations suggest that rapid permafrost degradation is increasingly common in the Arctic and is linked to warmer temperatures (Jorgenson et al. 2006). Feedbacks from terrestrial ecosystems are recognized as one of the largest sources of uncertainty in global climate models (Friedlingstein et al. 2006). Warming-induced permafrost

DOI 10.1007/s10040-012-0939-y

Published online: 20 December 2012

degradation may contribute to these feedbacks through a variety of mechanisms, including through altering the energy balance and vegetation dynamics (e.g., Sturm et al. 2001) as well as rates of microbial decomposition of soil organic carbon, which could release a large amount of soil carbon back into the atmosphere as CO_2 and CH_4 (Zimov et al. 2006; Schuur et al. 2009).

The mode of permafrost degradation in response to warming is highly variable (Jorgenson and Osterkamp 2005). In the Coastal Plain of Alaska where this study takes place, the permafrost is continuous yet the high volume of ground ice at the top of the permafrost also renders these areas susceptible to degradation (Nelson et al. 2001). Over successive freeze–thaw cycles, a polygonal network of ice wedges can form (Leffingwell 1915) that can push up the overlying soil, resulting in rims that surround low-centered polygons. When the ice wedges thaw and subside, they become troughs that surround high-centered polygons. Where topographic gradients are low and the active layer is thin, such polygonal landforms can greatly influence the microtopography and in turn, the hydrological storage capacity and drainage behavior of the region (Engstrom et al. 2005; Rowland et al. 2010). In these environments, topographic differences on the order of centimeters can be sufficient to alter the hydrology. For example, low-centered polygons often have standing water during the growing season (Liljedahl et al. 2012), whereas the middle regions of high-centered polygons are typically well drained (Woo and Guan 2006). Additionally, permafrost thaw is expected to alter the evolution of drainage networks, which in turn has the potential to change the volume and distribution of water. Since soil moisture is a key variable that affects vegetation and the surface energy balance in Arctic systems (Chapin et al. 2000), gaining an understanding of the controls on soil moisture spatiotemporal distribution is critical for quantifying ecosystem feedbacks to climate.

Because polygonal troughs often serve as pathways for water and nutrients (Woo and Guan 2006) and the soil-water saturation state influences redox state (Kögel-Knabner et al. 2010), the microtopographically controlled moisture distribution in low-gradient Arctic regions can also greatly alter the subsurface biogeochemistry that controls organic carbon decomposition. Several studies performed in thermokarst or polygonal ground features in Alaska have documented the control of topographic variability on active layer properties that influence the rates and mechanisms of organic content decomposition such as moisture content, pH and iron content (e.g., Lee et al. 2010, 2011; Zona et al. 2011; Lipson et al. 2012; Sommerkorn 2008).

Together, these studies indicate a few important findings that motivate this study: (1) topographic, hydrological and geochemical parameters that contribute to ecosystem-climate feedbacks can vary substantially over length-scales of several meters or less in permafrost regions and (2) many relevant terrestrial-ecosystem environmental variables are correlated with each other over space, suggesting the potential for using proxy measurements to provide information about the spatial distribution (or zonation) of suites of properties as well as about the interdependencies of system compartments (land surface, active layer, permafrost). Indeed, in a study focused on exploring microtopographic controls on Alaska Coastal Plain ecosystem functioning, Zona et al. (2011) recommended that 'future studies should explore more advanced methodologies which could integrate different scale measurements, taking the polygon structure into account in the investigation of carbon dynamics'.

Characterization of the properties within and coupling between land surface, active layer and permafrost and their joint controls on ecosystem functioning is challenging due to the varied nature and wide range of scales over which associated geomorphological, hydrological, and biogeochemical processes interact. Although point-based measurements can provide direct information about individual key properties (such as topography, active layer thickness, soil moisture and temperature, ground ice and aqueous geochemistry), their invasive nature and limited spatial extent often prohibit high-resolution quantification of property spatial distributions and inter-dependencies. Additionally, given that land-surface and subsurface variations can occur over length scales of a meter or less, adequately spaced conventional (point or wellbore-based) sampling methods also have a propensity to disturb fragile ecosystems, thereby rendering the samples less representative of in situ conditions. Exacerbating the characterization effort is the dynamic nature of the Arctic, where available soil moisture and hydrological connectivity vary dramatically with seasons (e.g., Hinkel et al. 2001a, b; Wright et al. 2009), which in turn affects thermal and biogeochemical rates and mechanisms (Sturtevant et al. 2012; Zona et al. 2011).

To circumvent the challenges described in preceding discussion, this study explores the combination of point measurements, which are direct but spatially sparse, with LiDAR and surface geophysical datasets, which are indirect but spatially extensive, for characterizing land-surface and subsurface variabilities and their linkages. The utility of LiDAR and surface geophysical datasets are explored using data collected during one field campaign, which was performed at the end of the 2011 growing season. As such, the findings are representative of the environmental conditions associated with that time period only. However, given the ability to now autonomously collect geophysical monitoring datasets (such as electrical resistivity tomography), the approaches explored in this study should be extensible for characterizing the temporal as well as spatial variability of land-surface and subsurface properties important for ecosystem-climate feedbacks.

LiDAR methods yield high-resolution (<1 m) topographic estimates, which can be used to quantify geomorphological features and thus the propensity for surface-water routing and drainage over large areas. LiDAR has been used extensively to map geomorphological or depositional features such as landslides (e.g., McKean and Roering 2004; Glenn et al. 2006), alluvial fans (Frankel and Dolan 2007) and channel beds (Cavalli et al. 2008) and have more recently been used to investigate geomorphology and its evolution in Arctic systems (Rowland et al. 2011).

 DOI 10.1007/s10040-012-0939-y

Whereas LiDAR provides information about land-surface variability, surface geophysical methods have the potential to provide information about subsurface property variability, including the active layer and the deeper permafrost. Significant advances in using geophysical methods to quantify hydrological and biogeochemical processes in shallow aquifers have been realized over the past decade (see reviews by Hubbard and Linde 2011; Hubbard and Rubin 2005; and Atekwana and Slater 2010). Several recent reactive transport-modeling studies have now also demonstrated the significant benefit of using geophysically obtained subsurface property estimates to improve the predictive understanding of shallow subsurface biogeochemical processes and system functioning (e.g., Scheibe et al. 2006; Wu et al. 2011).

Recent studies have also illustrated that geophysical methods can be useful for characterizing permafrost systems (e.g., Kneisel et al. 2008; Hauck and Kneisel 2008). Ground penetrating radar (GPR) data have been used for characterizing active layer thickness and moisture content (Brosten et al. 2006; Hinkel et al. 2001a, b; Monroe et al. 2007; Bradford et al. 2005; Steelman and Endres 2009; Steelman et al. 2010; Brosten et al. 2009; Westermann et al. 2010; Wollschläger et al. 2010). Both GPR and electrical resistivity methods have been successfully used to delineate regions having different quantities and types of ground ice (DePascale et al. 2008; Hauck et al. 2010; Yoshikawa et al. 2006). Surface-based (Harada et al. 2000) and airborne (Minsley et al. 2012b, b) electromagnetic approaches have also been used to map permafrost distribution. Electrical (Hilbich et al. 2008; Wu et al. 2012) and seismic (Hilbich 2010) methods have shown potential for mapping thaw fronts or assessing freeze–thaw dynamics. In spite of these advances, very few studies have attempted to use multiple geophysical methods to understand the variabilities of properties and interdependencies associated with different compartments of an Arctic ecosystem, including the active layer and deeper permafrost. Additionally, the use of geophysical data to delineate permafrost zonation of property that is potentially meaningful in terms of ecosystem-climate feedbacks has, to the authors' knowledge, not been explored.

This study explores the potential of combining LiDAR and multiple geophysical datasets to characterize and relate geomorphology and subsurface thermal and hydrogeochemical variability. The study was conducted near Barrow, Alaska, as part of a new Department of Energy (DOE) Next-Generation Ecosystem Experiments (NGEE-Arctic) project, which has a long-term goal of developing a process-rich ecosystem model that extends from the bedrock to the top of the vegetative canopy, where the evolution of Arctic ecosystems in a changing climate can be modeled at the scale of a high-resolution Earth system model. Critical for meeting this goal is the development of approaches to quantify land-surface properties that influence energy balance, and subsurface processes that influence microbial decomposition of organic carbon–in high resolution and over landscape scales, as is needed to refine process understanding and parameterize and validate the numerical models.

The specific objectives of this first NGEE-Arctic geophysical study are to: (1) to evaluate the utility of different geophysical approaches (including surface GPR, electrical and electromagnetic data) for providing information about variability in subsurface properties (such as moisture and active layer thickness) that potentially influence terrestrial-ecosystem feedbacks to climate at the Barrow NGEE-Arctic site; (2) to evaluate the potential of LiDAR and geophysical data to delineate land-surface and subsurface property zonation, respectively; and (3) to explore the linkage between subsurface and land-surface variability in tundra environments using geophysical and LiDAR datasets. If extant, such a linkage could provide a vehicle for upscaling and for estimating critical subsurface properties in high resolution and over large spatial scales as needed for numerical model initialization and validation.

Study site, methods and datasets

Study site and spatially nested acquisition campaign

The village of Barrow (71.3°N, 156.5°W) lies within the Alaskan Arctic Coastal Plain (USA), which is bordered on the north by the Arctic Ocean and on the south by the foothills of the Brooks Range. Permafrost at the site is continuous, ice-rich, and is present to depths greater than 350 m (Sellmann et al. 1975). This study was performed within the Barrow Environmental Observatory (BEO; Fig. 1), which is located approximately 6 km east of Barrow. The terrestrial landscape of the region includes a mosaic of thaw lakes, drained thaw lake basins and interstitial polygons (Hinkel et al. 2007); the landscape is characterized by low topographic relief, low hydraulic gradient and shallow depths (<1 m) to the top of the permafrost. Historic (1901–2007) mean annual air temperature is −12 °C and mean annual precipitation is 113.5 mm, with the majority falling as rain during the short summer. Soils in the BEO are generally classified as Gelisols, which are characterized by an organic-rich surface layer underlain by a horizon of silty clay to silt-loam-textured-mineral material and a frozen organic-rich mineral layer.

The study site is located directly west of a previously NSF-supported biocomplexity flooding and draining experimental study site (e.g., Goswami et al. 2011; Lipson et al. 2012). LiDAR data collected in 2005 (Fig. 1) revealed that land surface at the study site is dominated by polygonal features. Indeed, visual identification of at least three different types of polygons, including high-centered polygons (ice-wedge polygons having the highest topographic value in the center), low-centered polygons (polygons having the lowest topographic value in the center), and transitional polygons. The presence of these different polygons motivated the choice of the study site, as different polygons could potentially indicate different states of permafrost degradation and moisture distribution.

 DOI 10.1007/s10040-012-0939-y

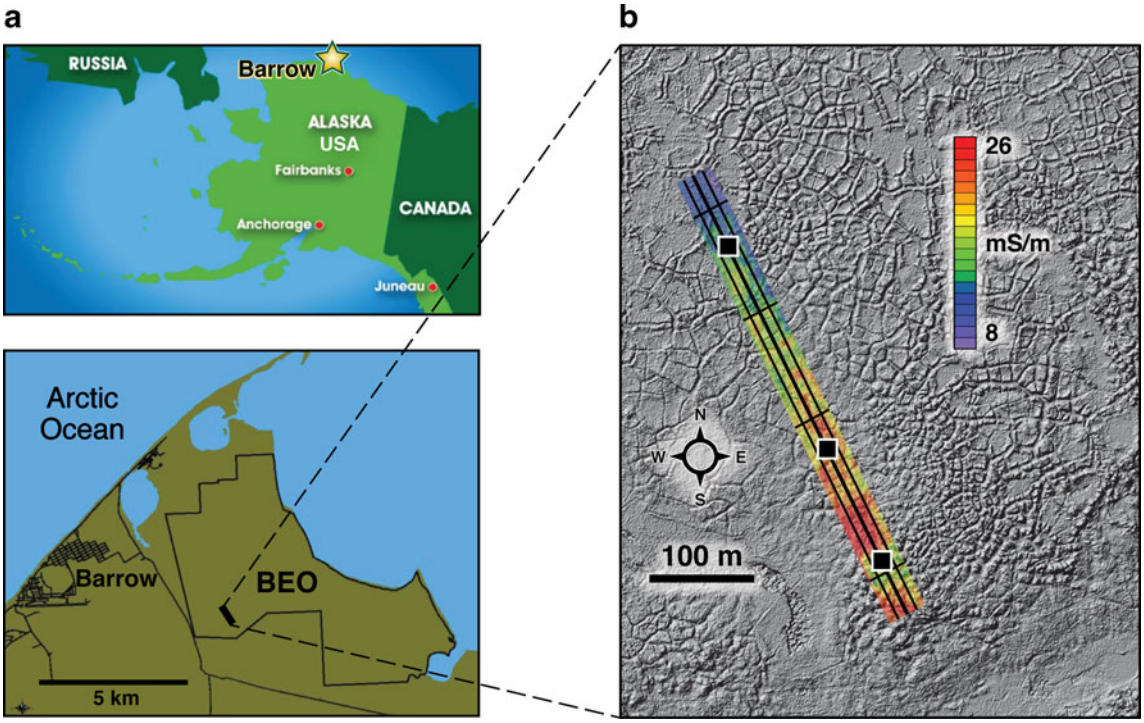

Fig. 1 **a** Location of Barrow, Alaska, USA; **b** Location of the Barrow Environmental Observatory (*BEO*) near Barrow; **c** Study site location, with boundaries identified by the spatial extent of the electromagnetic (EM) grid. *Colors* indicate the electrical apparent conductivity values from the EM data, which are superimposed over the LiDAR-based elevation image. The location of the centerline GPR/ERT transect is indicated by the *heavy solid center line*; the additional parallel and perpendicular GPR lines are shown by the other *solid lines*, and the locations of detailed sampling sites are indicated by *black boxes*

A ~47-5 m-long by 40-m-wide NW–SE-trending study zone was defined to encompass these three different types of polygons.

Geophysical and point measurements were collected within the study site the week of September 24–October 1, 2011. The average daily air temperatures ranged between 0 °C at the beginning of the week to −2.7 °C at the end of the week, with the highest temperature of 1.1 °C and the lowest of −6.6 °C. Snowfall up to 4 cm/day was intermittent. During the week of the campaign, the surface waters transitioned from thawed state to a partially frozen state. However, the soils remained unfrozen, and thus the campaign was representative of the end of the growing season. The cold and thus hard ground surface facilitated the acquisition of surface geophysical data in a manner that did not appear to disturb the fragile tundra.

The campaign included the acquisition of a suite of nested datasets geared toward assessing the spatial variations of subsurface properties at the end of the growing season; details of each of the datasets are provided in the sections to follow. The boundaries of the study site were defined by the spatial extent of the grid of electromagnetic (EM) data as shown in Fig. 1. Surface ground-penetrating radar (GPR) and electrical resistance tomography (ERT) geophysical data were collected along a centerline transect and several additional GPR transects were collected along transects that extended parallel and perpendicular to this centerline (Fig. 1). Active layer thickness, soil temperature, and soil moisture measurements were collected using uniform spacing along the centerline and two parallel GPR transects located on either side of the centerline. Detailed sampling sites were established along the grid centerline (Fig. 1), where various measurements or samples were collected at tight spatial spacing (on the order of meters and less), including soil/core samples, active layer thickness, soil temperature, and soil moisture. Soil samples were subsequently analyzed to characterize texture, aqueous geochemistry, carbon and nitrogen content, and moisture content.

LiDAR and geophysical datasets and analysis

The LiDAR and surface geophysical methods that were used for this study are briefly reviewed in this section. Additional information about the LiDAR, GPR, ERT, and EM methods are provided in the Appendix. Along the geophysical transects, as well as at all point-measurement stations, a global positioning system (GPS) was used to measure latitude, longitude and elevation using a Topcon GRS-1 Real Time Kinematic (RTK) GPS. Positional accuracy during data collection was sub-centimeter in both vertical and horizontal directions.

LiDAR data

LiDAR data were acquired on October 4, 2005 over the study site and processed to yield a digital elevation model with a spatial resolution of 0.5 m. Information about the LiDAR data acquisition and processing are provided in the Appendix. Three metrics were extracted from the

 DOI 10.1007/s10040-012-0939-y

processed LiDAR data to characterize the geomorphology of the polygonal land surface: directed distance (m), local slope (m/m), and wavelet curvature (1/m). Directed distance was measured from the elevated ridgelines of the polygonal features (Gangodagamage et al. 2011). In high-centered polygon regions, the distance was calculated from the center of the polygons to the trough area along the flow path in all directions. The directed distance associated with transitional and low-center polygons was calculated from the elevated ridgeline toward the polygonal center and then toward the outside trough area of the polygons along the flow-path direction. Directed distance was also used as a scale parameter to characterize the slope and curvature attributes in terms of ensemble averages. Local slope was computed by considering a region composed of 9 (3×3) grid cells and curvature was computed by convolving a Gaussian kernel with the elevation dataset and by performing landscape smoothing at 1.5-m scale (Lashermes et al. 2007).

Ground penetrating radar (GPR)

Surface, common-offset GPR transects were collected at the study site along three ~475-m-long parallel transects and along several ~40-m-long perpendicular transects using the Sensors and Software Pulse Ekko 1000 system with both 450 and 900 MHz antennas (Fig. 1). An odometer was used to control trace spacing of 10 cm; each trace represented a stack of eight individual traces. The sampling interval for the 450 MHz was 200 ps and for the 900 MHz, was 100 ps. Minimal processing of the common offset lines included zero-time adjustment, bandpass filtering, automatic gain control, conversion of travel time to depth, and correction for microtopographic variations using elevation data measured along the transects. Conversion of the GPR signal travel time to the top of the permafrost and back to the ground surface was based on an average velocity of the active layer obtained from the analysis of several common midpoint (CMP) gathers that were also collected at various locations in the study site using step-out increments of 0.05 and 0.1 m. The two-way time of the radar signal, down and back from the key reflector (which was identified as the interface between the active layer and the permafrost based on comparison with active layer probe depth measurements), was picked using Promax software and exported for analysis. The GPR data were displayed as two-dimensional (2D) vertical plane transects.

Electrical resistance tomography (ERT)

A ~475-m-long ERT profile was collected along the study site centerline (Fig. 1) using a 112-electrode AGI Super-Sting R8 system, a dipole-dipole survey geometry with 0.5-m electrode spacing, and a roll-along acquisition strategy. The largest distance between the closest injection and potential electrode was 18 m, while the largest distance between the two injection (or potential) electrodes was 3 m. Low quality measurements were removed from the acquired data set, including signals associated with measured potentials less than 3 mV and those associated with faulty electrodes. The electrode locations were adjusted for elevation and inverted for electrical resistivity using CRTomo, which is a smoothness-constraint inversion code that is based on a finite-element algorithm (Kemna 2000). As described in the Appendix, the discretization of the model varied with position and no corrections for temperature dependency were made. The obtained mean absolute difference between the calculated and measured data was ~12 %. The obtained electrical resistivity values were displayed as a 2D vertical plane.

Electromagnetic (EM) data

An EM38-MK2 was used to collect electromagnetic datasets along 14 transects that were each 475 m long and that were located 1.5 m from each other. The EM38-MK2 simultaneously acquires data using two transmitter receiver coil separations (1 and 0.5 m). The EM grid was collected twice using both horizontal and vertical coil orientations and collected with the instrument located ~0.05 and 0.1 m above ground surface respectively. Acquisition was performed using an external control unit that allows for synchronization of the acquisition with positioning from the GPS navigation system. Tool zero adjustment was performed using the instrument protocols twice per day (Geonics 2009). The acquired data were inverted at each location to obtain a one-dimensional (1D) subsurface resistivity model using the least-squares based algorithm EM1DFM (Farquharson 2000) and by enforcing the model to be as close as possible to a starting layered model defined on prior structural information from an ERT profile; details about the inversion parameters are provided in the Appendix. The raw and inverted electrical conductivity values were displayed as 2D plan view depth-averaged maps; an example of the raw data is shown in Fig. 1.

Point measurements

Several different types of point measurements or samples were collected within the study site: one set was collected over a 'grid', using uniform spacing along the three long GPR transects. The other set was collected using a non-uniform spacing within the three detailed sampling sites, which were located along the centerline transect (within the boxes shown in Fig. 1).

Grid-based point measurements

Thaw depth was measured at 300 locations using a 20-m sampling interval along the outside two long GPR transects, a 3-m sampling interval along the centerline transect, and a 0.5-m sampling interval within the detailed sampling sites (refer to Fig. 1). The measurements were collected using a steel T-handled tile probe labeled with centimeter gradations starting at the bottom of the probe. Because the acquisition campaign occurred at the end of

 DOI 10.1007/s10040-012-0939-y

the growing season, the thaw depth measurements are considered to be equivalent to the active layer thickness (ALT). At all locations where ALT was measured, the soil permittivity and soil temperature were also measured. In situ dielectric permittivity measurements were obtained using a soil-moisture-Trase-system time domain reflectometer (TDR) with two 20-cm waveguides placed 5 cm apart and with a central frequency of approximately 3 GHz. For this study, the TDR-obtained dielectric permittivity values were used only as a proxy for water content, with low values indicating relatively dryer soils and higher values representing relatively more moist soils. However, investigations using Barrow soils indicate a good relationship between dielectric permittivity and water content as described by Eq. 2 (Engstrom et al. 2005). Soil temperatures were measured using an EXTECH Instruments EA15 Thermocouple with two type K bead wire temperature probes, which have a temperature range from −30 to 300 °C with a 0.1° resolution. Both temperature sensors (T1 and T2) were fixed to the tile probe used to measure thaw depth thickness. T2 was located at 10 cm shallower than the base tip of the probe and T1 was located 20 cm above the base tip of the probe.

Point measurements collected in detailed sampling sites

In addition to the 'grid' of uniformly sampled measurements described in the preceding, three detailed sampling sites were established along the grid centerline (boxes in Fig. 1), where measurements or samples were collected at spacings ranging from 0.5–11 m. Measurements included soil dielectric permittivity, soil temperature and ALT, all collected using the techniques already described. Additionally, a peat corer, which had a ~10-cm-long tip, was used to collect soil samples from the thawed layer. Because this tip could not penetrate through the permafrost, the peat corer could only retrieve the soils that existed from the ground surface to about 10 cm above the permafrost (or in approximately the top 40 cm). Three core samples were obtained at each location for different subsequent analyses, including: (1) texture, gravimetric moisture, cation analysis, and carbon/nitrogen analysis; (2) geophysical laboratory analysis; and (3) microbiological analysis. This study includes analysis of core samples collected for the first suite of measurements. Descriptions of geophysical laboratory studies using the second set of cores are described by Wu et al. (2012), and microbiological analysis of the third suite of cores is in progress (Jansson et al. 2012). Where vertical differentiation was visible, samples were collected at different depths. Photographs were taken of all soil samples and the samples were split for subsequent analysis.

Laboratory analysis of the soil samples was performed to assess texture, moisture, and geochemical properties. The samples were dried over a period of about 1 week in a freeze dryer until no further weight loss was observed. The weight difference before and after the freeze-dry process was used to calculate gravimetric moisture content. Because the soil samples recovered were not cohesive, it was challenging to estimate the sample volume and, thus, bulk density, which is needed to convert the gravimetric water content to volumetric water content. Acquisition of frozen cores from the same study sites is currently in progress to remedy this limitation. Subsequently, the freeze-dried samples were sub-sampled for texture and carbon/nitrogen analysis. Soil textural analysis on 18 samples was performed using the pipette method by Soil and Plant Laboratory, Inc. (SPL) of San Jose, California (USA), in accordance with the procedures outlined in Klute (1986). All samples were analyzed for carbon and nitrogen concentrations from bulk soils. Subsequent to freeze drying, soil samples were cleaned of any live organic matter and then sieved through a 2-mm sieve to remove any rocks. Roots were removed using tweezers, and the soil samples were then coned, quartered and then ground for ~24 h using a ball-bearing roller. The bulk soil samples were subsequently transferred to a scintillation vial and rendered into ~20–45-mg foil balls for analysis. Atropine was used to develop a standard calibration curve, and duplicate analysis of carbon and nitrogen isotopes were performed for each soil sample using a Carlo Erba NC2100 analyzer.

Major cation analysis was performed on pore water retrieved from the core samples. This analysis was viewed as opportunistic as the samples were not ideally preserved to represent in situ conditions with confidence. The soil samples were diluted with deionized water for pore-fluid extraction. For each sample, 1–2 g of the bulk soil was diluted at 1:5 weight ratio using deionized water and the diluted samples were continuously mixed on a shaker for 3 days. After mixing, the supernatant of each sample was extracted and filtered through 0.2-micro filters. The filtered samples were subsequently measured for (diluted) electrical conductivity and then acidified and analyzed with inductively coupled plasma-mass spectrometry (ICP-MS, Perkin Elmer) for major and trace cations, including Ca, Na, Mg, Fe, Al, Si, K, Mn, Cu, and Zn.

Statistical methods for assessing and comparing datasets

Statistical analysis of the datasets included three components: (1) exploratory data analysis to identify correlations among different geophysical datasets and subsurface properties, (2) cluster analysis to identify possible spatial zonation based on LiDAR data and geophysical attributes, and (3) statistical testing to delineate geomorphic, thermal, hydrological and geochemical characteristics associated with each identified zone.

The exploratory data analysis considered co-located point measurements and geophysical datasets at more than 100 points. The main focus was to establish correlations between the geophysical attributes (i.e., two-way radar travel time, electrical resistivity) associated with the geophysical centerline traverse and subsurface properties from the point measurements (e.g., moisture, ALT, temperature). Linear curve fitting, which was found to be acceptable for this analysis, was used to compute the

 DOI 10.1007/s10040-012-0939-y

correlation between geophysical attributes and subsurface parameters.

Cluster analysis of the LiDAR metrics and geophysical attributes was performed to explore for the presence of land-surface and subsurface zonation, respectively, with the motivation that developing easy ways to identify such zonation using spatially extensive datasets could be useful for guiding in-field detailed sampling and for point measurement upscaling. Additionally, comparison of land-surface and subsurface zonation, if it exists, offers a means to evaluate linkages between hydrogeomorphology and subsurface hydrogeochemical-thermal properties, all of which are important for gaining a predictive understanding of terrestrial ecosystem-climate feedbacks. In-field observations suggested the presence of at least three different types of polygonal ground: low-centered polygons (in the southern portion of the study site), high-centered polygons (in the northern portion of the study site), and 'transitional' polygons in the middle portion. As such, clustering analysis was performed on both the LiDAR-extracted metrics (directed distance, slope and curvature) as well as the geophysical attributes (electrical resistivity and GPR two way travel time) by a priori defining three clusters.

Cluster analysis was performed to assess whether three unique combinations of the LiDAR-obtained metric distributions existed. The analysis was performed on the metrics extracted from the LiDAR data over a 60-m-wide rectangle that encompassed the center geophysical transect. The analysis included calculating the mean statistics and covariance structure of the input slope, curvature, and directed distances from the LiDAR data and then computing the posterior probabilities using a maximum likelihood classifier for all of the pixels that belonged to one of three classes. Based on the posterior probabilities, the input pixels were classified into one of three bins based on the highest probability score. The classifications were then 'mapped' back into space to explore the spatial variation of LiDAR metric clusters.

In a similar manner, unsupervised clustering was used with the geophysical attributes to identify if unique combinations of subsurface geophysical attributes existed. Given overlapping Gaussian-shaped distributions of the geophysical attributes, a Gaussian mixture model-based clustering algorithm (Hastie et al. 2001) was used, which is expected to perform well under such conditions. Three clusters were prescribed based on visual observations described earlier. All of the geophysical attributes along the centerline were used in the cluster analysis, including the electrical resistivity from ERT and from inverted EM signals and the two-way travel time of the GPR signal to the base of the active layer. The electrical resistivity values from ERT and inverted EM signals were divided into shallow (less than 0.2 m, representing the active layer) and deep (1.0–2.0 m, representing the permafrost) categories. To honor each geophysical attribute consistently, the attributes were normalized by their respective mean and standard deviations. The MCLUST package (Fraley and Raftery 2012) from the statistical computing software R (R Development Core Team 2010) was used for the clustering, which uses an expectation maximization algorithm that computes and maximizes the expectation of log-likelihood iteratively (Hastie et al. 2001). The identified classifications were then projected back into space to explore if coherent spatial variations of subsurface geophysical attribute clusters existed.

After subsurface zones were identified through cluster analysis of geophysical data, the subsurface characteristics of each zone was explored through analysis of the detailed point measurements that were collected in each of the zones, including soil temperature, soil-moisture content, ALT, carbon content, and iron and potassium concentrations. Visualization of the distribution of each attribute in different zones was facilitated using boxplots, which show the distribution of the parameters as well as their mean value and outliers. The significance of the distribution of these properties as a function of zone was quantified and tested by multiple comparison statistical testing, including one-way analysis of variance (ANOVA) with the null hypothesis that there is no zonation difference, and Tukey's pairwise comparison test (Christensen 2002).

Results and discussion

Grid-based point measurements

The probe data revealed the thin nature of the active layer in this region: the average depth to the top of the permafrost was 36 cm (with a 37 cm range from 21 to 58 cm), which is similar to results found through nearby studies (Shiklomanov et al. 2010). GPS-measured elevation averaged 5.14 m (with a 71 cm range from 4.79 to 5.53 m); LiDAR estimated and GPS-measured elevations compared favorably. Soil temperatures in the grid varied between 1.1 and 1.9 °C and relative dielectric permittivity values varied between 3.8 and 87.8. Figure 2 provides examples of grid-based point measurements along the centerline geophysical transect and reveals some general trends. The thickest active layer zones often appear beneath local topographic lows, and these regions also tend to have higher soil temperatures and higher dielectric permittivity values (indicative of higher moisture). The correspondences suggest that the troughs and the middles of low-centered polygons are likely associated with more standing or flowing water than surrounding areas. The surface water can lead to increased moisture content in the deeper soils and, thus, higher heat retention and conduction, which could deepen the active layer beneath, relative to surrounding zones (e.g., Engstrom et al. 2005; Lee et al. 2010).

LiDAR metric and cluster analysis

Figure 3a and c show select examples of the spatial distribution of the LiDAR-extracted slope and curvature

 DOI 10.1007/s10040-012-0939-y

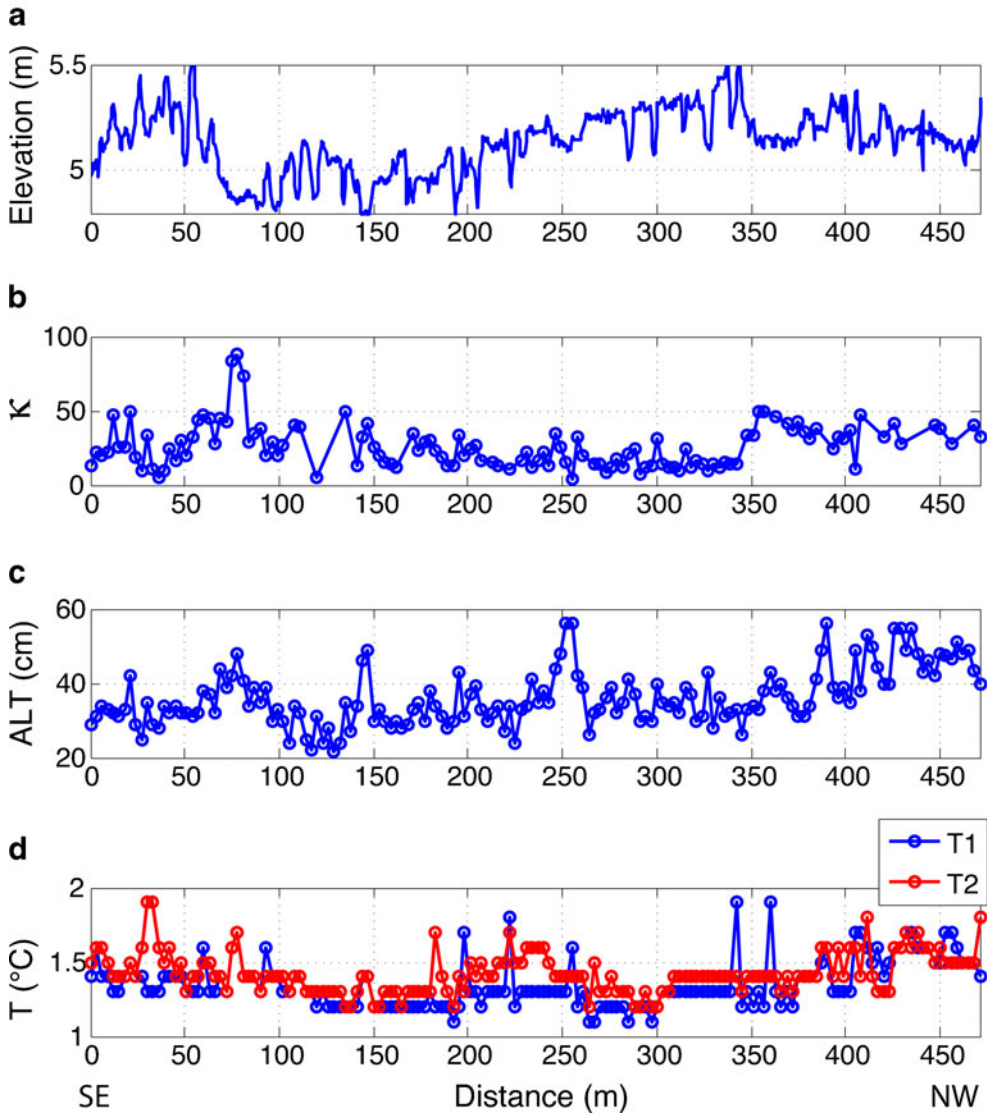

Fig. 2 Point measurements collected at uniform intervals along the centerline traverse shown in Fig. 1. **a** Elevation (m above sea level); **b** dielectric permittivity (κ), which is indicative of soil moisture content; **c** active-layer thickness (*ALT*); and **d** temperature at two depths (*T1*: shallow temperature, *T2*: deeper temperature)

near the south end of the center geophysical transect; the corresponding mean values of slope and curvature (<S> and <C>) are plotted in Fig. 3b and d as a function of directed distance. Figure 4a shows the spatial distribution of the LiDAR-extracted metrics over the entire study region. Figure 4b shows a three-dimensional (3D) cross-plot of the LiDAR metrics, which reveals three distinct clusters. Spatial translation of those identified clusters is shown in Fig. 4c. Figure 5a, b shows mean slope and curvature as a function of directed distance for representative areas within each of the LiDAR- identified geomorphological zones.

Analysis of the LiDAR metrics and associated geomorphological clustering reveals the presence of three distinct zones that varied in a coherent manner from south to north in the study region (zones 1, 2 and 3; Fig. 4c), and which reflected the geomorphic controls on drainage. Zone 1, the region of high-centered polygons, has the highest slope, highest negative curvature and highest positive curvature measurements. The high slope and negative curvature values are located near the centers of the high-center polygons, which facilitate flow dispersion from the center area of the high-centered polygons to the outside trough area. The exterior polygonal areas in zone 1 have higher slopes and higher positive curvatures compared to other zones, which also facilitate the water and sediment transport. These metrics suggest that under the hydrological conditions associated with this end-of-the-growing season field campaign, zone 1 has the highest relative drainage potential of the three zones. Zone 3 reveals lower slope and lowest curvature distributions over length scales ranging from 5 to 30 m. Lower positive curvature values close to the polygon center suggests a low tendency for drainage and a higher tendency for water to stagnate; moderately low slopes also support this interpretation. The zone 2 LiDAR metrics mainly reveal

 DOI 10.1007/s10040-012-0939-y

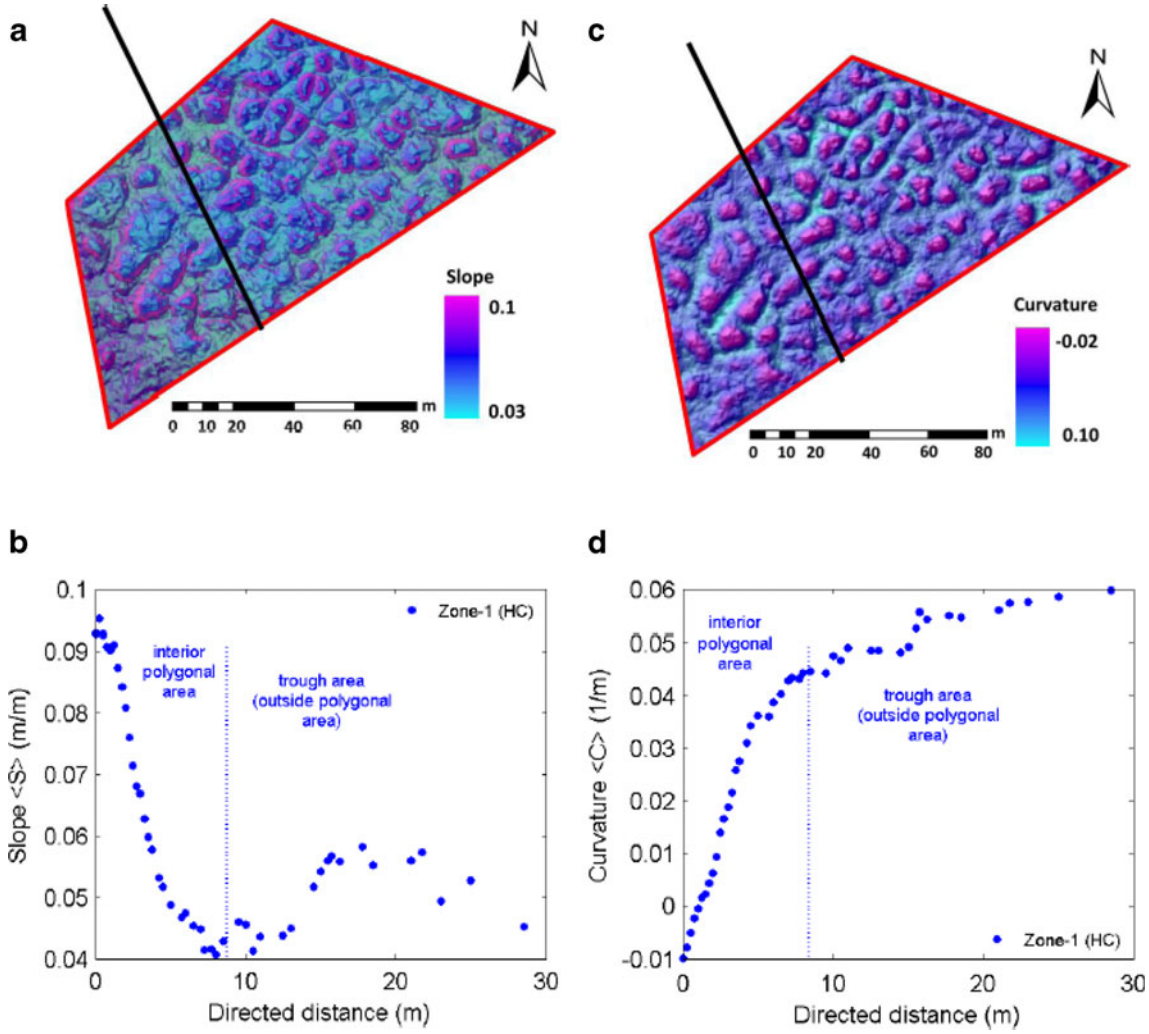

Fig. 3 Examples of LiDAR-extracted metrics from the southern end of the study site: **a** slope as a function of directed distance from polygon center, plan view; **b** mean slope versus directed distance; **c** curvature from polygon center, plan view; **d** mean curvature from polygon center. The *black lines* in **a** and **c** illustrate the location of the centerline geophysical transect. Slope units are m/m and curvature units are 1/m

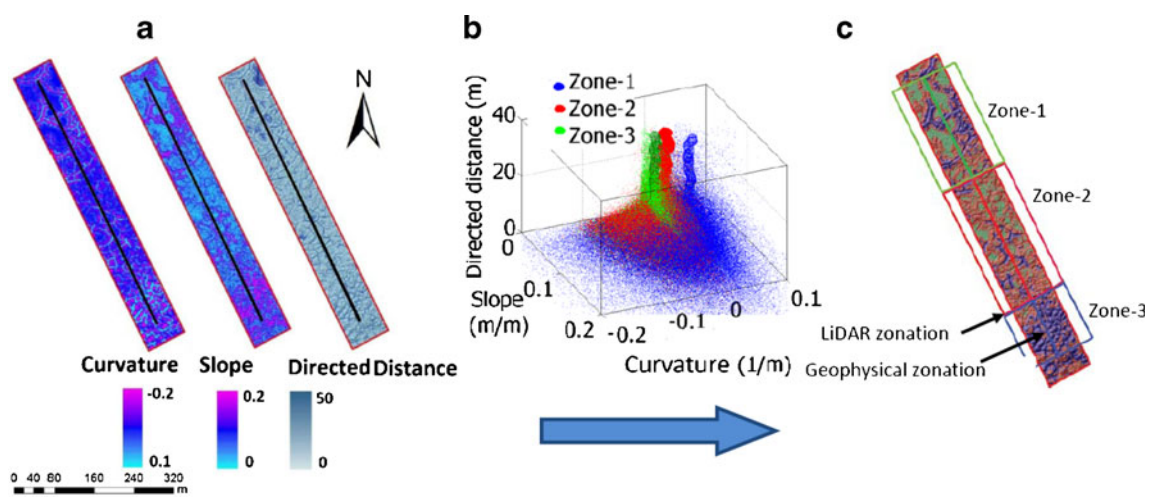

Fig. 4 Cluster analysis of LiDAR-based metrics reveal geomorphic zonation: **a** spatial distribution of LiDAR-based slope, curvature, and directed distance fields surrounding the *black centerline* geophysical transect; **b** slope, curvature, and directed distance values, plotted in 3D space, which reveal three distinct clusters, **c** Spatial distribution of the points in **b**, where the *blue, red and green boxes* identify the spatial distribution of three distinct LiDAR-based geomorphological zones. The geophysical zonation is described in Fig. 9

 DOI 10.1007/s10040-012-0939-y

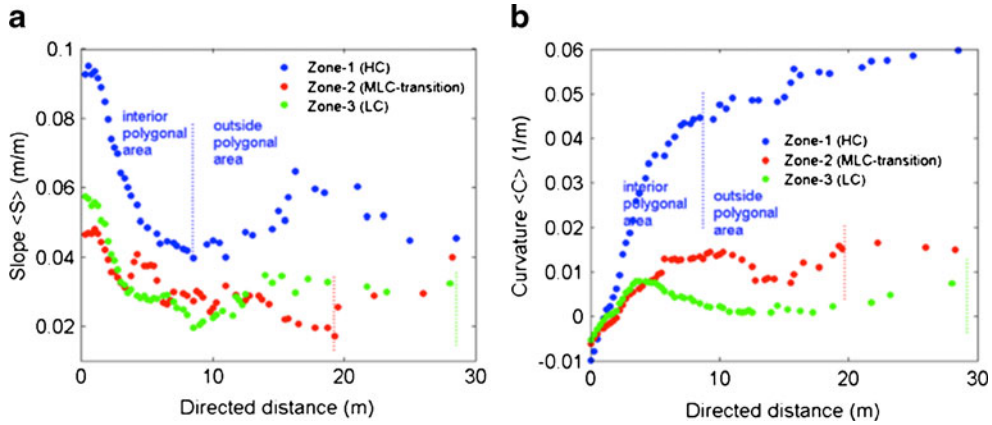

Fig. 5 LiDAR-extracted mean **a** slope and **b** curvature versus directed distance for a southern region of the study area (zone 1), the middle region (*zone 2*) and the northern region (*zone 3*). The *colored vertical lines* indicate the estimated polygon diameters for each zone based on the extracted metrics

moderate slope and moderate curvature distributions. This analysis suggests that zone 2 is a transition zone that has some characteristics that are shared with both zone 1 and zone 3, suggesting a relatively moderate drainage potential. From these metrics, the mean polygon diameters associated with each zone were estimated (as is indicated by the colored vertical lines on Fig. 5a, b); the average diameter of the zone 1 polygons was 9 m, of zone 2 was 19 m, and of zone 3 was 29 m.

Geophysical data analysis

Analysis of the GPR, EM and ERT data reveals their utility for characterizing the active layer and underlying permafrost. A fence diagram constructed using the processed 900 MHz GPR data is shown in Fig. 6a, which was converted into depth using an average velocity of 0.055 m/ns obtained from analysis of the four CMP gathers located between 0 and 220 m along the profile. As recognized by many previous studies, Fig. 6a illustrates

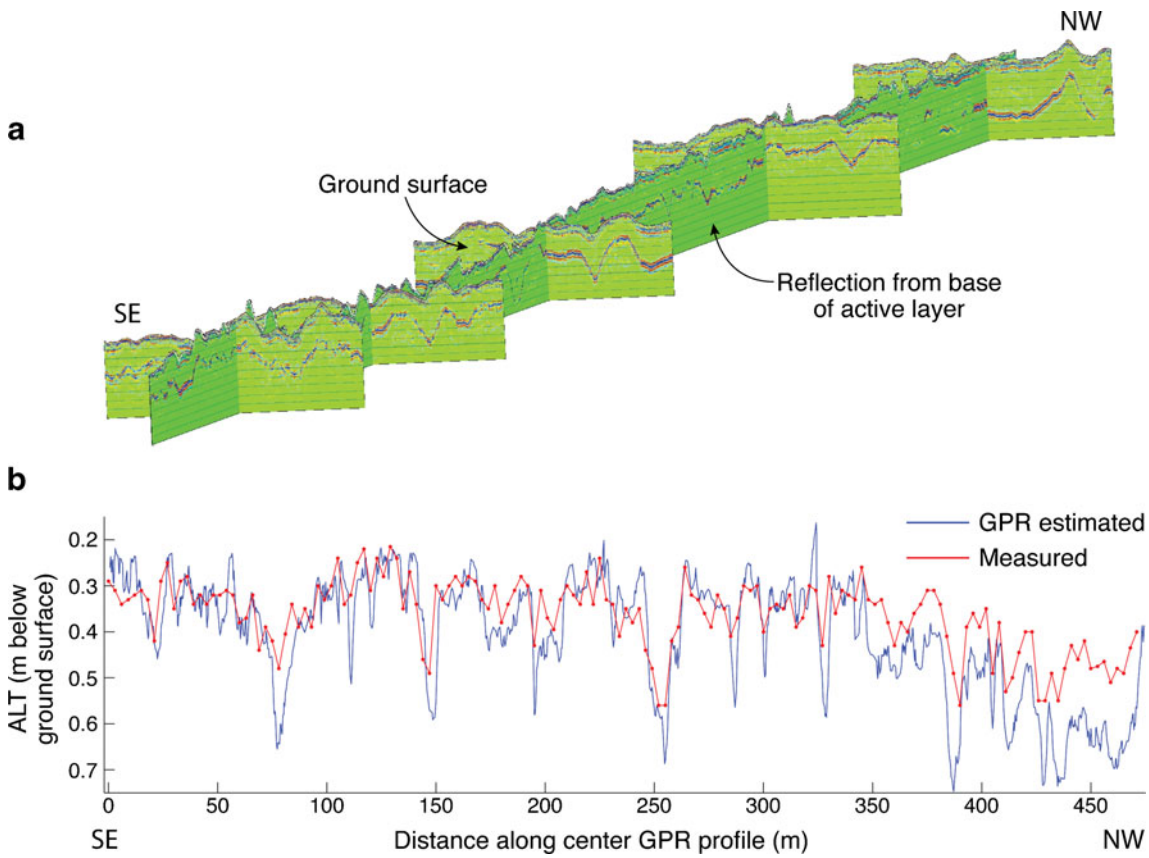

Fig. 6 **a** Fence diagram of the 900 MHz GPR data, clearly revealing the reflection associated with the base of the active layer; **b** comparison of 900 MHz *GPR-estimated* and probe-*measured* base of active layer along the centerline traverse

 DOI 10.1007/s10040-012-0939-y

that the interface between the active layer and the permafrost represents a significant dielectric contrast that yields a coherent radar reflection. Due to the presence of a wet and attenuating active layer and a strong contract in dielectric properties at the active layer-permafrost boundary at the end of the growing season, there was little signal penetration beneath the base of the active layer. Indeed, the 450 MHz profiles reveal very similar responses to the 900 MHz radar responses shown in Fig. 6a. Figure 6a shows that a single, constant velocity value that was used to transform the GPR two-way travel times into depth, yielded a depth to the base of the active layer that agreed extremely well with the ALT point measurements made by the active layer probe (R^2=0.74, Fig. 6b). The fit is less optimal on the north end of the transect (at distances greater than 340), where water was pooled in the middle of the low-centered polygons; improvements in the fit would likely be realized if the GPR velocity in water and shallowest soils in this region were incorporated into the time-to-depth conversions. This analysis reveals the utility of GPR at this site for providing high resolution and accurate estimates of active layer thickness in a non-invasive manner, as has been documented by other studies, including those conducted near Barrow (e.g., Monroe et al. 2007; Hinkel et al. 2001a, b).

The inverted ERT profile is shown in Fig. 7a with two different y-axis scales to permit inspection of both shallow and deeper electrical resistivity variations. The ERT reveals shallow resistivity values in the active layer that range between ~30 and 400 Ohm.m; the transition to high resistivity values below this zone agrees well with the base of the measured active layer (superimposed on Fig. 7a as a black line). The correlation between active layer resistivity and dielectric permittivity (Fig. 7b, R= 0.52) and the recognition that dielectric permittivity relates to water content (Eq. 2) indicate the sensitivity of electrical conductivity to moisture content in the Barrow active layer. The good correlation (R=0.72) between resistivity and probe-measured ALT indicates the relationships between resistivity, ALT and moisture content. The deeper high-resistivity regions in Fig. 7a are interpreted to indicate the presence of ground ice content and structure (i.e., ice wedges or massive); this hypothesis is being confirmed through drilling. The lateral variability in the thickness of these deeper, high-resistive features is significant along the profile (from 0.5 to more than 5 m)

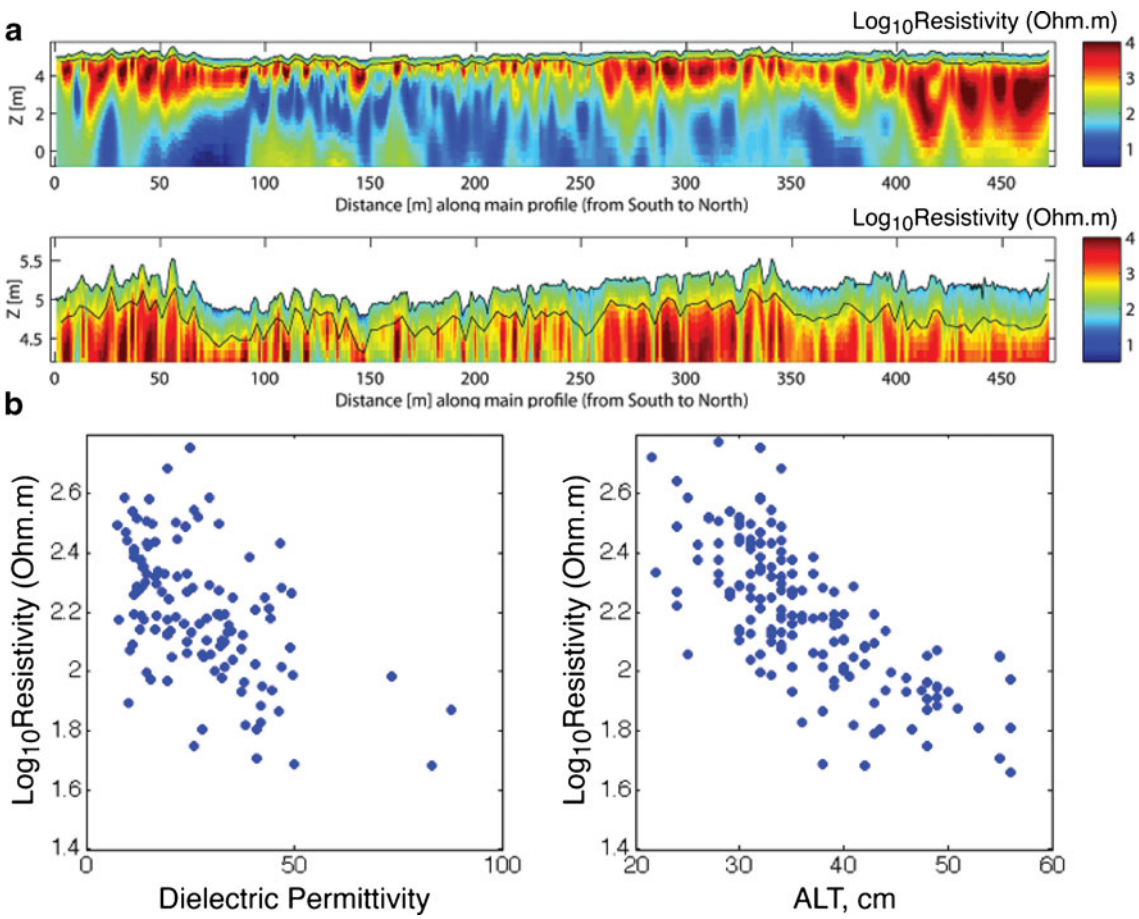

Fig. 7 Electrical resistivity tomography (ERT) and comparisons with point measurements. **a** ERT images along the main profile shown over a large depth interval, with the *top image* showing the full depth range and the *bottom* showing a close-up of the active layer (*black line* indicates the probe-measured base of active layer); **b** Mean of the logarithm of the resistivity imaged in the top 20 cm of the ERT versus dielectric permittivity and the probe-measured base of active layer

 DOI 10.1007/s10040-012-0939-y

and also locally. Very localized resistive features (>~2,500 Ohm.m) that appear to be ice wedges are often visible below troughs (e.g., at 146 m), high-centered polygons (e.g., at 293 m) and low-centered polygons (e.g., 411 m). Massive ice in the permafrost is interpreted to be present at the north end of the transect (at distances >400 m) based on the high resistivity responses in that region. At other deep locations along the transect, very low resistivity values (as low as ~10 Ohm.m at some locations) are observed. Such low values are likely indicative of high salinity, unfrozen and/or low-resistivity clay material. Additionally, these low resistivity values are more pronounced and shallower (above the actual sea-level) in the interval between a distance of ~80 and 260 m along the profile, which corresponds to the lowest topography elevations along the profile and is located on the edge of a large channel/drainage system that connects to the ocean. Ongoing analysis of recently recovered core data is expected to be useful for characterizing the texture, salinity and ice content of the permafrost. Analysis of the ERT data suggests its utility for providing quantitative information about active layer moisture content and thickness as well as for potentially characterizing ground ice variability and its relationship to active layer and microtopographic variability.

A map view of the apparent (i.e., not inverted) electrical resistivity obtained from the EM38 using the 1 m coil separation distance and collected in horizontal and vertical mode is shown in Fig. 8b, c respectively; the elevations at the corresponding locations are also shown for comparison (Fig. 8a). Figure 8d shows the electrical resistivity distribution at various depths obtained from inverting the EM data at each location for a 1D model. Inspection of the apparent electrical resistivity data (Fig. 8b, c), suggests that the measurements collected in horizontal mode (which is more sensitive to shallower variations than the vertical mode) reveal larger apparent resistivity values than the vertical mode, particularly between the distances of 0 and 400 m. This indicates that some low resistivity features are present in the deepest part, which is consistent with the results from the ERT image. This is also confirmed by the resistivity

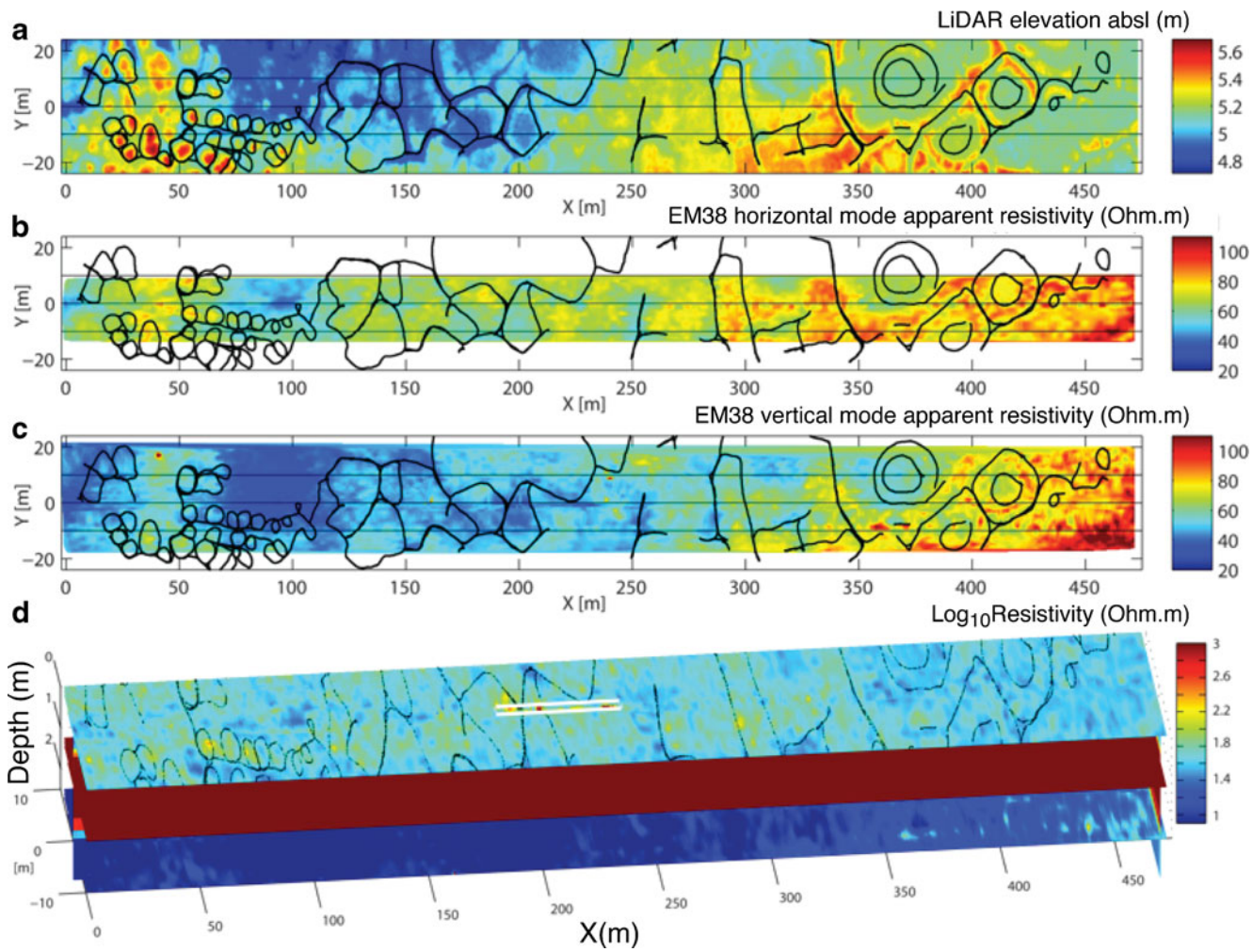

Fig. 8 Comparison of LiDAR data with raw and inverted EM data. **a** Plan view of LiDAR elevation and of the apparent electrical resistivity measured from EM38 using a 1 m coil spacing in **b** horizontal and **c** vertical mode. **d** 3D model of inverted electrical resistivity that fits the measured EM38 data. On all figures, the *black lines* show troughs observed in the field. The *white line* **(d)** represents a zone where data are particularly noisy due to collection of EM data near a region where ERT data were concurrently being collected

 DOI 10.1007/s10040-012-0939-y

distribution obtained from inversion of the EM signals (Fig. 8d). Inversion results indicate that obtained resistivity values in the top layer show consistent variations with moisture content variations along the profile (not shown), while the variability in the deeper layers shows a similar large trend to the LiDAR elevation data (Fig. 8a). This demonstrates that the measured EM signals are sensitive to both the active layer and permafrost regions.

Geophysical data cluster analysis

Cluster analysis was performed using several geophysical attributes, including ERT-based electrical resistivity averaged over shallow and deeper depth ranges, the two-way travel time of the GPR signal down and back from the active layer-permafrost interface, and electrical resistivity from EM data associated with a shallow and deeper zone. The cluster analysis revealed that geophysical data could be used to identify unique combinations of geophysical attribute distributions. Figure 9a shows the pairwise scatterplots of the elevation and geophysical attributes; this scatterplot is equivalent to the 3D crossplot shown in Fig. 4b for the three LiDAR attributes, although since multiple attributes are considered here, it is difficult to display in multi-dimensional space. Although the elevation was not used in the cluster analysis, it is shown in Fig. 9a to illustrate its correlation to some of the geophysical attributes, due to the control of microtopography on drainage and thus shallow system functioning in this Arctic Coastal Plain system. The colors in Fig. 9b indicate the spatial translation of the three identified clusters back into space along the centerline transect compared to the geophysical attribute and elevation values along the transect. Figure 9a, b indicates that there are distinct geophysical attribute and elevation ranges associated with the different zones. For example, when the members of the 'green cluster (shown in Fig. 9a) are translated back into space (Fig. 9b), the members are predominantly located along the south end of the transect (between distances of 0 and 70 m) and are associated with relatively high elevation, high ERT resistivity values in the shallow and deeper section, and relatively low (or fast) two-way GPR travel times to the base of the active layer. In contrast, when members of the identified 'blue' cluster are translated back into space, they are predominantly located along the north end of the line, and are associated with relatively low shallow ERT resistivity values, high deep ERT resistivity values, and high (or long) two-way GPR travel times to the base of the active layer.

The cluster analysis suggests that, in addition to using the geophysical data to characterize active layer and permafrost properties in high resolution, the ensemble of geophysical attributes identifies coherent subsurface zonation. The cross plots in Fig. 9a reveal that the correlation between the GPR travel time and shallow ERT resistivity is consistent with Fig. 7b, which is reasonable because of their joint dependence on ALT. It also reveals the correlation between elevation and deep

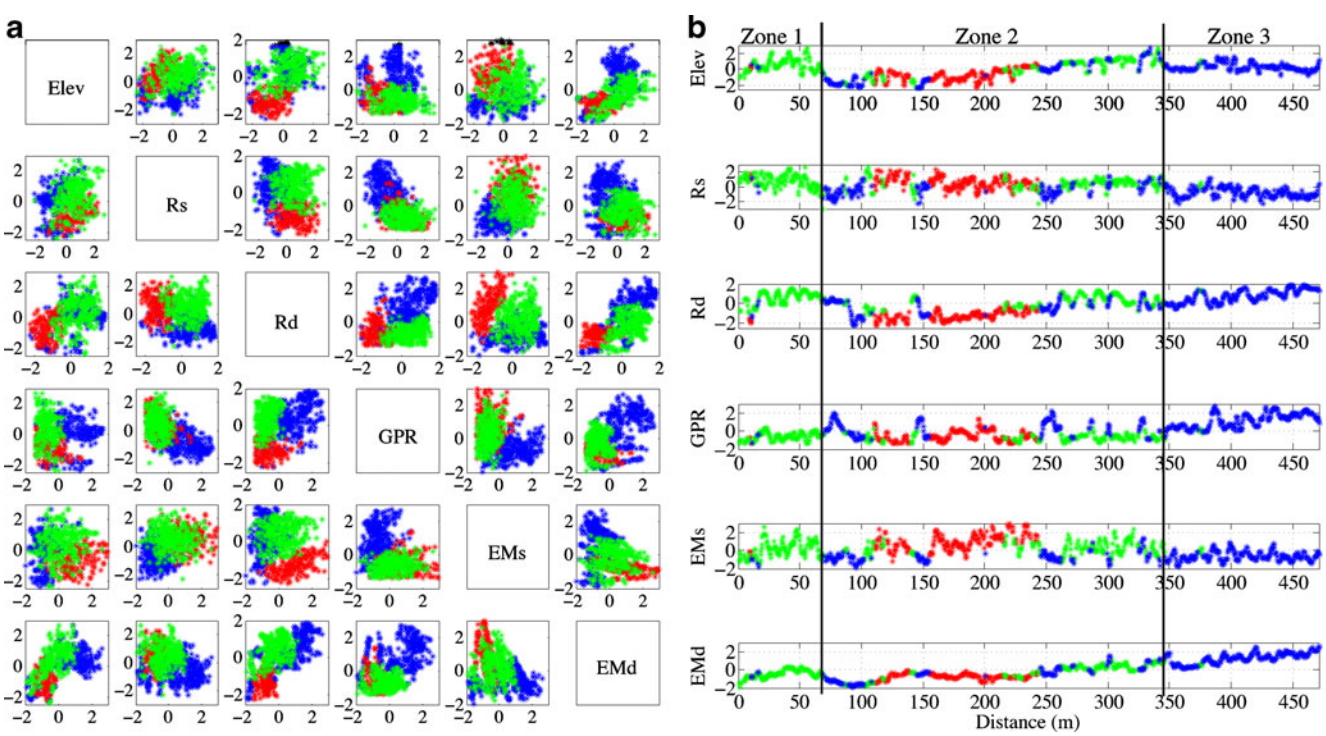

Fig. 9 Geophysical data cluster analysis: **a** pairwise scatterplots of elevation and geophysical attributes (*Elev* elevation, *Rs* shallow ERT resistivity, *Rd* deep ERT resistivity, *GPR* two-way travel time to base of active layer, *EMs* shallow EM resistivity, and *EMd* deep EM resistivity); **b** spatial translation of the clusters along the centerline transect, where the three colors (i.e., *green, blue and red*) represent the three identified clusters. The two *black lines* (**b**) indicate the boundaries between the LiDAR-identified surface zones. Elevation and geophysical attribute units are normalized as described in the text and are thus unitless

 DOI 10.1007/s10040-012-0939-y

resistivity from the EM data. Figure 9a shows that the three clusters are most pronounced when resistivity from deep ERT and EM resistivity are considered, which are sensing the permafrost. When the pairs include only consider shallow (active layer) attributes (shallow resistivity from ERT and EM and GPR travel time), the 'green' and 'red' clusters overlap significantly. This suggests that both active layer and permafrost variability contribute to the identified clusters. The translation of the cluster information to space (Fig. 9b) reveals spatially coherent subsurface zonation, where zones 1 and 3 are distinct but where zone 2 is mixed. Zone 1 is characterized by high resistivity values (obtained using both ERT and EM methods) in the active layer and low GPR travel time, whereas zone 3 has low resistivity (obtained using both ERT and EM methods) and high GPR travel time. Comparison of the three geophysically defined subsurface zones with the LiDAR-based surface zones (Fig. 4c) reveals the similarity of the subsurface and geomorphic zonation.

Detailed point data

After establishing the existence of reasonable correlations between geophysical attributes and hydrogeological attributes (e.g., active layer thickness and dielectric permittivity indicative of soil-water content) and establishing the presence of geophysically based subsurface zonation, statistical analysis of measurements collected within the three detail sampling sites (refer to Fig. 1 for location) was performed to explore if the three zones were associated with distinct thermal, hydrogeological, and geochemical property variations.

Figure 10 shows the locations of the core data collected within each of these three detail sampling sites as a function of geomorphic position. The figure shows that for each detailed site, samples were collected across geomorphic features, including polygonal centers, troughs, and their associated rims. Both low-centered polygons and high-centered polygons were sampled. The LiDAR imagery associated with the three study sites and the soil core locations are also shown in Fig. 10, revealing the different polygonal expressions at the three sites. Comparison of the detailed LiDAR imagery (Fig. 10), the site-scale LiDAR view (Fig. 1) and the LiDAR-based zonation analysis (Fig. 4c) suggests that the detailed sampling sites are representative of their surrounding areas. The LiDAR imagery confirms the visual observations made during the field campaign, suggesting that zone 1 is dominated by high-centered polygons and zone 3 by low-centered polygons. Zone 2 is a transitional zone that has less well defined low-centered polygons relative to zone 3.

Figure 11 shows a subset of the statistical analysis of the detailed site subsurface point data as a function of

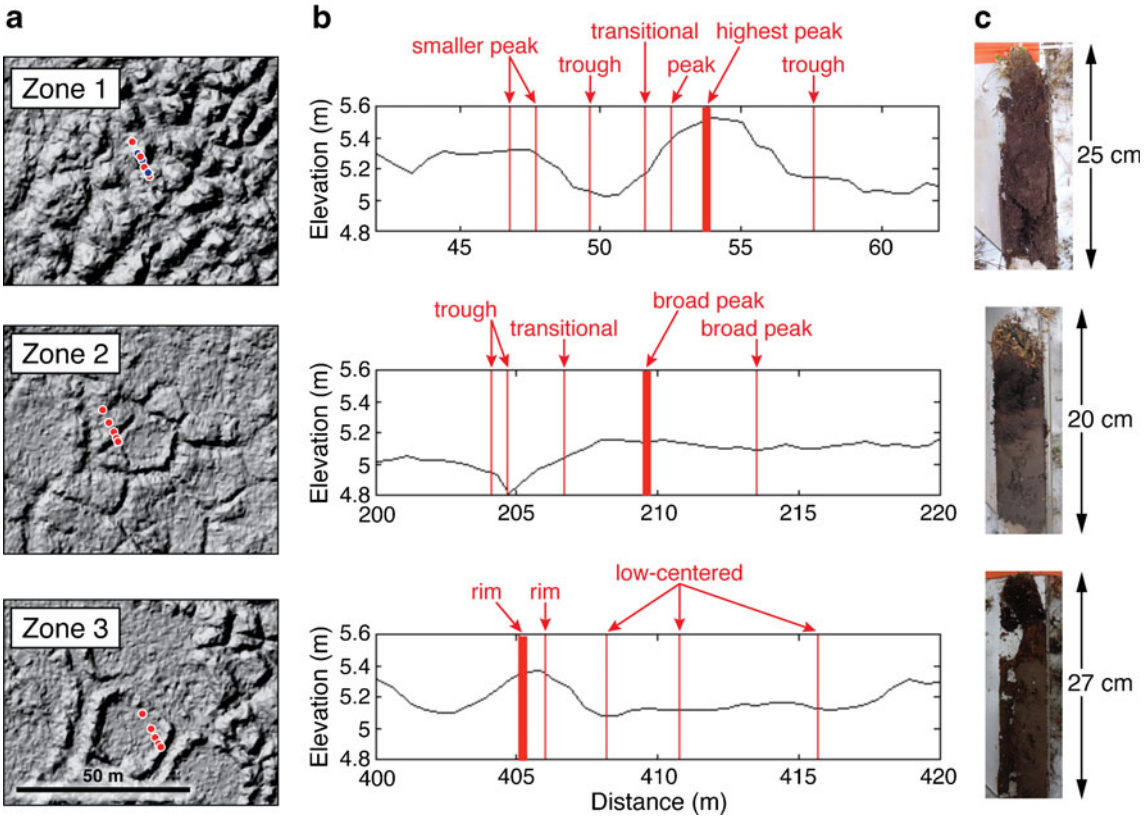

Fig. 10 **a** Plan view LiDAR detail imagery; **b** cross-sections of three detailed study sites showing associated core locations (*red lines*) as a function of geomorphic position; **c** core photographs associated with the *heavy red vertical lines* in the middle figures. Top: zone 1; *Middle*: zone 2; *bottom*, zone 3

 DOI 10.1007/s10040-012-0939-y

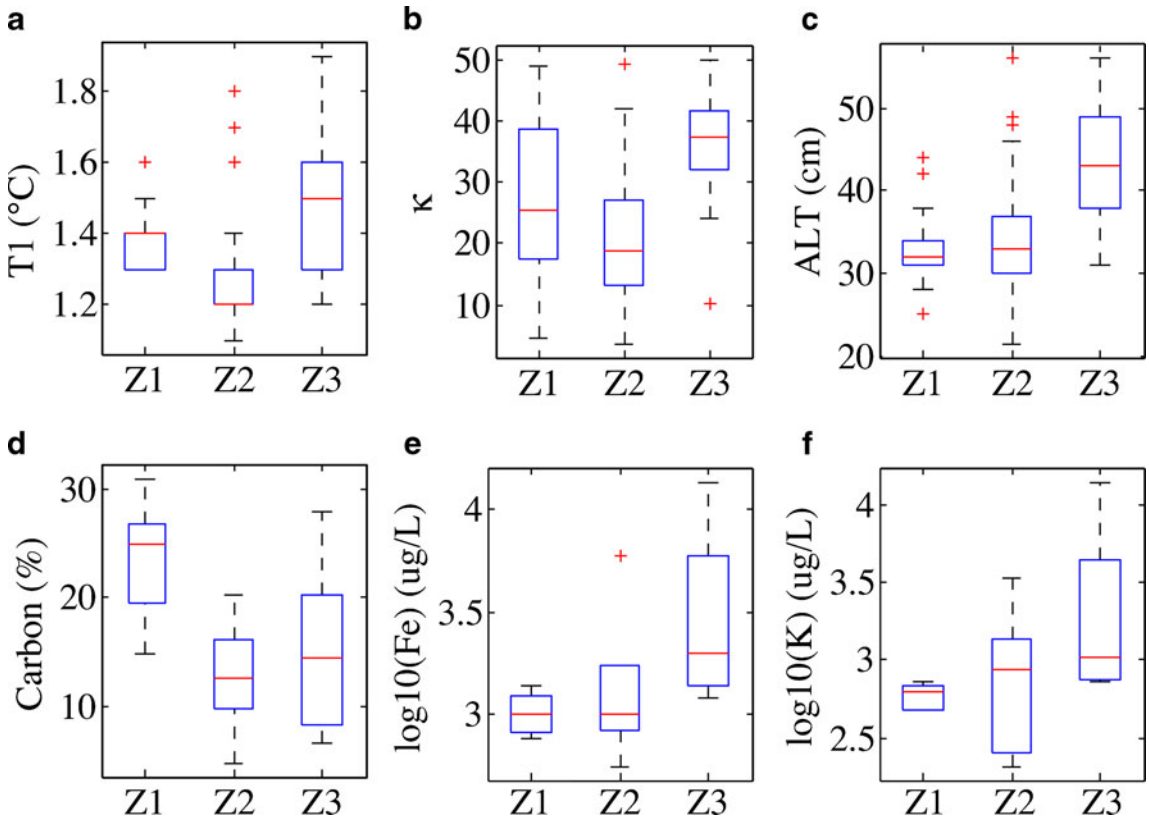

Fig. 11 Box plots of some of the point measurements collected in the detailed sampling sites (whose locations are shown by *boxes* on Fig. 1), illustrating variations in hydrological, thermal, and geochemical variations (see Table 1) as a function of geophysically identified zones. The *box* represents the 25th and 75th percentiles, the central *red line* is the median, and the *whisker-lines* indicate the 99 % interval. *Red crosses* indicate outliers

zone, which were analyzed to assess if thermal and hydrogeochemical properties varied as a function of geomorphology (i.e., high versus low-centered polygon). To primarily characterize mineral soil variations, the analysis discussed here was performed using soil samples collected from depths beneath the vegetation or peat layer with the sample length ranging from 10 to 18 cm. The box plots display the mean value and distributions of a subset of these point measurements, and Table 1 shows *p*-values from statistical tests conducted using the datasets shown in Fig. 11. This analysis reveals that many of the subsurface property distributions did indeed vary as a function of geomorphological zone, including: moisture content, soil temperature, cation concentration, carbon content as well as their ratios, soil texture, active layer depth, and elevation. Notably, the mineral soil texture was relatively constant across the zones, with 15 of the 17 samples assessed for texture characterized as a sandy clay loam. However, the vertical soil profile (organic layer plus mineral soil) was observed to be significantly different among the three zones. In general, cores recovered in zone 1 were light brown over their entire depth, lacked a clear organic-mineral soil interface, and had a thin vegetation layer that persisted up to 5 cm below ground surface. In zone 2, all the cores had a clear interface between the dark organic soil and mineral soil; this interface occurred about 8 cm below ground surface. In zone 3, the vertical soil profile included organic soils and a root zone that extended to 18 cm below ground surface. Representative images of the active layer cores from the three zones are shown in Fig. 10.

Examples of zone-based characteristics revealed by Fig. 11 include: the transitional zone 2 is dryer and cooler than the other zones; zone 3 soils (low-centered polygons) are the most moist, have the deepest average active layer thickness, and have the highest iron and potassium pore water concentrations; and zone 1 (high-centered polygons) reveals more carbon content in the mineral soils relative to other zones. The one-way ANOVA *p* values (Table 1) performed using the data shown in Fig. 11 suggest that there is a significant difference among all parameters as a function of zone except for K and Fe. The high *p* values in K and Fe may be attributed to the non-ideal preservation of the samples prior to analysis. The *p* values from the pairwise companion test confirm that zones 1 and 3 indeed have distinct parameter distributions (except for K and Fe) while the transitional zone 2 is similar to zone 1 for ALT, and to zone 3 for carbon. Although assessing geochemical variations at one snapshot in time is not sufficient to characterize what is expected to be a seasonally dynamic environment, this first analysis provides evidence that the subsurface zonation identified through cluster analysis of geophysical attributes is meaningful in terms of subsurface hydrological, thermal, and geochemical properties.

 DOI 10.1007/s10040-012-0939-y

Table 1 p values from the ANOVA test, and Tukey's pairwise comparison test for pair zone 1 and zone 2 (pair 1–2), pair zone 1 and zone 3 (pair 1–3) and pair zone 2 and zone 3 (pair 2–3)

	ANOVA	Pair 1–2	Pair 1–3	Pair 2–3
Temperature	3.99E-13[b]	7.85E-04[b]	8.74E-03[b]	2.11E-13[b]
ALT	3.37E-11[b]	8.48E-01	6.93E-08[b]	2.72E-10[b]
κ[a]	3.11E-07[b]	6.81E-02[b]	6.74E-03[b]	1.52E-07[b]
Carbon	8.89E-03[b]	9.89E-03[b]	7.08E-02[b]	8.19E-01
Potassium (K)	1.66E-01	9.38E-01	1.57E-01	3.01E-01
Iron (Fe)	1.18E-01	8.46E-01	1.04E-01	2.84E-01

[a] κ relative dielectric permittivity

[b] p values smaller than 10 %

Synthesis

The datasets and analysis discussed previously have revealed that:

- The LiDAR-based metrics can provide information about geomorphological variations (such as slope, curvature, and directed distance of polygons) that can be used to indicate the drainage propensity of the land-surface regions in high resolution and in a non-invasive manner. Cluster analysis of the LiDAR-based metrics reveals that the land surface can be divided into three geomorphic regions, ranging from high-centered polygons in the southern region to low-centered polygons in the northern region.
- Geophysical attributes can provide high-resolution information about subsurface active-layer variability (including moisture content and active-layer depth) and potentially ground ice and permafrost variability in a high-resolution and minimally invasive manner.
- Cluster analysis suggests that combination of multiple high-resolution geophysical attributes can be used to identify subsurface zonation. Analysis of subsurface point measurements within these zones suggests that the geophysically defined zones have unique distributions of hydrological, thermal, and geochemical properties.
- There is a strong correspondence between land-surface zonation (obtained from LiDAR cluster analysis) and subsurface zonation (obtained from geophysical cluster analysis), suggesting the dependencies between micro-topography/geomorphology, active layer, and permafrost. Table 2 provides a summary of the zonal-based characteristics discussed in this study.

Conclusions

As part of a new, long-term DOE Next-Generation Ecosystem Experiments (NGEE-Arctic) project, an evaluation of the value of combined LiDAR and surface geophysical measurements was performed for characterizing land-surface and subsurface variabilities and their spatial relationships. The study was carried out near Barrow, Alaska (USA), at the end of the 2011 growing season in a region that displayed different polygonal ground characteristics. High-resolution LiDAR data had been previously collected over the study site, and surface ERT, GPR and EM data were collected in conjunction with a variety of point measurements, including active-layer thickness, soil temperature, and moisture-content measurements/proxies. Soil samples were collected and analyzed for moisture content, texture, carbon and nitrogen content, and cation concentrations.

Table 2 Land surface, active layer, and permafrost characteristics identified in this study and qualitatively described as a function of zone. Details associated with the measurements are provided in the text and in Figs. 2, 5, 9 and 11

Characteristic	Zone 1	Zone 2	Zone 3
Land surface			
Elevation	Most variable	Lowest mean	Highest mean, least variable
Geomorphology	High-centered polygon	Transitional	Low-centered polygon
Mean polygon diameter	9 m	19 m	29 m
Drainage potential[a]	High	Moderate	Low
Active layer and permafrost			
Active layer thickness	Moderate	Moderate	Thickest
Soil moisture content	Most variable	Most dry	Most wet
Soil temperature	Warmer	Coolest	Warmer
Ground ice content and form[a]	Moderate/wedges	Low/wedges	High/massive
Carbon content %	Highest	Lowest	Moderate
Cations[b]	Low K and Fe	Moderate K and Fe	Highest K and Fe
Dominant soil texture	Sandy clay loam	Sandy clay loam	Sandy Clay loam

[a] Interpreted but not yet confirmed

[b] High measurement uncertainty

 DOI 10.1007/s10040-012-0939-y

Analysis of the LiDAR data revealed its utility for providing geomorphic metrics that are potentially useful for characterizing land-surface drainage potential such as slope, curvature and directed distance. Cluster analysis of these three LiDAR metrics revealed the presence of three clusters that had unique LiDAR 'signatures'. Translation of these clusters to space showed that the clusters were distributed spatially and systematically into three zones that corresponded with geomorphological characteristics, including a high-centered polygon area, a low-centered polygon area, and a transitional area.

Geophysical analysis revealed that the GPR and ERT data were of high quality and were useful for providing high-resolution information about active layer and permafrost properties as well as for identifying meaningful subsurface zonation. Simple processing of the GPR data illustrated that these data can be used to obtain accurate estimates of the active layer thickness. ERT inversions revealed electrical resistivity variations in the active layer and permafrost. Electrical resistivity variability in the active layer correlated with active-layer thickness and dielectric permittivity (an indicator of moisture), whereas electrical resistivity variability in the permafrost is hypothesized to be associated with ground-ice heterogeneity, a hypotheses that is currently being tested through analysis of recently recovered core. Inversion of the EM data was most challenging due to its non-unique nature. Still, the EM raw and inverted data yielded useful information about the electrical conductivity distribution that was useful for inferring active layer and permafrost variations. The analysis suggests the potential of the geophysical data for characterizing subsurface properties (such as moisture content and active layer thickness) that influence energy balance and soil respiration, both important for assessing terrestrial feedbacks to climate. Particularly novel in this study is the use of multiple types of geophysical datasets to explore spatial variability within different compartments of the Arctic system (active layer and permafrost) and to help reduce ambiguity in the interpretation of the data. Ongoing research is focused on new Bayesian estimation approaches that will improve the ability to estimate subsurface hydrochemical properties using the geophysical data (e.g., Wainwright et al. 2012) and on improved EM inversion for quantitative subsurface characterization in Arctic environments.

Cluster analysis of the geophysical attributes revealed that the subsurface can also be grouped into three zones. Analysis of subsurface measurements collected from within these zones revealed distinct hydrological, thermal, and geochemical parameter distributions. This analysis highlights the potential usefulness of the geophysical data to identify meaningful subsurface hydrogeochemical/thermal zonation that can be used to guide sampling, to aid in upscaling smaller-scale information to larger scales, and to provide estimates of subsurface parameters (and their dynamics) that are useful for initializing and validating reactive transport models.

The strong correspondence between the LiDAR and geophysical data zonation suggests that there is a close linkage between microtopography, active layer, and permafrost variability at the study site during the end of the growing season. Because the strong control of microtopography on coastal-plain tundra functioning is recognized, this finding is not surprising. However, to the authors' knowledge this is the first study to document the similarity of the subsurface and land-surface variability in high spatial resolution and primarily in a non-invasive manner. These findings suggest the potential of using LiDAR- and geophysical-based information to characterize land-surface and subsurface properties (respectively) that are likely to play a role in landscape deformation and drainage and a cascade of related processes that result in modified energy balance and soil fluxes of carbon and methane–all of which are important for quantifying ecosystem evolution and feedbacks to climate. The study also suggests how different types of data can be used to understand heterogeneity of ecosystem compartments (land surface, active layer, permafrost) and importantly, their coupling that leads to overall ecosystem functioning.

Although further studies are needed to explore the utility of this approach in different permafrost environments and especially over time, these findings open the way for future research focused on using combined geophysical and remote-sensing datasets to estimate land-surface and subsurface permafrost terrestrial-ecosystem properties in a minimally invasive and high-resolution manner. Additionally, because geophysical data can be collected in a time-lapse mode, they offer the potential to understand how subsurface properties or states (such as snow accumulation, active layer depth, aqueous geochemistry, soil moisture and temperature, and permafrost characteristics) vary over both space and time. When used in combination with LiDAR, this further opens the door for understanding the dynamic interdependencies between permafrost ecosystem compartments (microtopography, active layer, and permafrost). Such high-resolution estimates and process understanding is critical for initializing, parameterizing, and validating process-rich models that can simulate feedbacks between terrestrial processes and climate in evolving Arctic ecosystems.

Acknowledgments The Next-Generation Ecosystem Experiments (NGEE Arctic) project is supported by the Office of Biological and Environmental Research in the DOE Office of Science. This NGEE-Arctic research is supported through contract number DE-AC0205CH11231 to Lawrence Berkeley National Laboratory and through contract DE-AC05-00OR22725 to Oak Ridge National Laboratory. Funding for Alessio Gusmeroli was provided by the Alaska Climate Science Center, funded by Cooperative Agreement Number G10AC00588 from the United States Geological Survey. The authors thank Margaret Torn and Christina Chastanha (both LBNL) for providing guidance on the core sample carbon analysis; Bob Busey (University of Alaska at Fairbanks) for the graduated tile probe design; Drs. A. Kemna and M. Weigand at University of Bonn for providing the 2D complex resistivity imaging code; and Roman Shekhtman of UBC for providing the EM inversion code EM1DFM. Logistical support in Barrow was provided by UMIAQ, LLC. The contents of the study are solely the responsibility of the authors and do not necessarily represent the official views of the author's institutions.

 DOI 10.1007/s10040-012-0939-y

Appendix: LiDAR and surface geophysical background

Brief descriptions of the LiDAR, ground penetrating radar (GPR), electrical resistance tomography (ERT) and electromagnetic methods are provided in this section.

LiDAR data

LiDAR data were collected over the Barrow site, Alaska, by AeroMetric on October 4, 2005 at an altitude of approximately 600m above mean ground elevation using an Optech 70kHz Airborne Laser Terrain Mapper (ALTM 30/70) on board a twin engine Cesna 310 aircraft. The system was configured with a differential global positioning system (DGPS) and 200-Hz inertial measurements units (IMU) were used to improve the accuracy of ground data. LiDAR data were processed by PND Engineers Inc. The data were post-processed utilizing Optech's REALM software, which first computes a 2-Hz Post Processed Kinematic DGPS trajectory, then integrates the IMU data for a final smoothed best estimate of trajectory (SBET). SBET data were then integrated with the LiDAR pulse data to obtain a final x, y, z "point cloud" dataset. Classification of point cloud data for bare-earth was performed using Terrascan software. The horizontal and vertical accuracy is approximately 0.30 and 0.15m respectively. A digital elevation model at 0.5-m spatial resolution was created using GRASS software by importing x, y, z point cloud data and performing linear interpolation.

Ground penetrating radar (GPR)

GPR methods use electromagnetic energy at frequencies of ~10MHz to 1GHz to probe the subsurface. At these frequencies, the separation (polarization) of opposite electric charges within a material that has been subjected to an external electric field dominates the electrical response. GPR systems consist of an impulse generator which repeatedly sends a particular voltage and frequency source to a transmitting antenna. The most common ground surface GPR acquisition mode is surface common-offset reflection, in which one (stacked) trace is collected from a transmitter-receiver antenna pair that is pulled along the ground surface. When the electromagnetic waves in the ground encounter a contrast in relative dielectric permittivity (also known as dielectric constant), part of the energy is reflected and part is transmitted deeper into the ground. The reflected energy is displayed as 2D profiles that indicate the travel time and amplitude of the reflected arrivals; such profiles can be displayed in real time during data collection and can be stored digitally for subsequent data processing.

The velocity of the GPR signal can be obtained by measuring the travel time of the signal for various known separation distances between the transmitter and the receiver. For surface GPR, this is accomplished by successively moving the transmitter and receiver apart at specific increments to yield what is called a common midpoint (CMP) gather. Analysis of the arrival time of the reflections in this CMP gather can be performed to estimate the radar propagation velocity. This velocity can be used to convert the GPR profiles, which are recorded as distance versus travel time, into distance versus depth sections. A review of GPR methods applied to hydrogeological applications is given by Annan (2005).

The propagation phase velocity (V) and signal attenuation of the electromagnetic wave are controlled by the dielectric permittivity (or dielectric constant, κ) and the electrical conductivity of the subsurface material through which the wave travels. At the high frequency range used in GPR, the velocity in a low electrical conductivity material can be related to the dielectric permittivity, as

$$\kappa \approx \left(\frac{c}{V}\right)^2 \qquad \text{(Eq.1)}$$

where c is the propagation velocity of electromagnetic waves in free space (Davis and Annan 1989). Due to the sensitivity of dielectric permittivity to moisture content (Birchak et al. 1974; Topp et al. 1980), the travel time and thus velocity of the radar wave are largely controlled by water content. A petrophysical relationship developed using Barrow soils that are similar to those of the study site to relate volumetric water content (θ) to dielectric permittivity is (Engstrom et al. 2005):

$$\theta = -2.5 + 2.508\kappa - 0.03634\kappa^2 + 0.0002394\kappa^3 \qquad \text{(Eq.2)}$$

However, due to the typical presence of significant organic materials and variable freeze states in Arctic soils, other factors must also be considering when using dielectric measurements to quantify soil-water content (e.g., Watanabe and Wake 2009).

Electrical resistance tomography (ERT)

Electrical resistivity methods are probably more frequently used for shallow subsurface studies than any other geophysical method. Resistivity is an intrinsic property of a material indicating its ability to resist electrical current flow; it is the inverse of electrical conductivity. At low frequencies measured, energy loss via ionic and electronic conduction dominates. Ionic conduction results from the electrolyte filling the interconnected pore space (Archie 1942) as well as from surface conduction via the formation of an electrical double layer at the grain-fluid interface (e.g., Revil and Glover 1998). Most resistivity surveys utilize a four-electrode measurement approach, where current is injected between two electrode and electrical potential difference measured between two others, while varying the location of electrodes along the profile and the distance between them (e.g., Binley and Kemna 2005). Modern multi-channel geoelectrical equipment decrease acquisition time by injecting current through two electrodes and measuring the potential difference (voltage) signal between several pairs of

 DOI 10.1007/s10040-012-0939-y

electrodes and using electrodes alternatively as both current and potential electrodes, a method now referred to as electrical resistivity tomography (ERT). A review of this method is provided by Binley and Kemna (2005).

Data quality is typically initially assessed through creating an apparent resistivity (pseudo-section) section, which is developed following Ohm's Law with information about the injected current, the measured potential difference and the geometric factor (which is a function of the electrode configuration) and through assuming uniform subsurface conditions. Further processing involves the estimation of the spatial distribution of resistivity that reproduces in a given range of uncertainty the measured data. Inversion of ERT data typically involves iterative minimization of the misfit between measured and calculated data by optimizing two- or three-dimensional electrical resistivity models (e.g., Kemna 2000; Ramirez et al. 2005; Guenther et al. 2006).

For the inversion of the ERT data described in the previous section Electrical resistance tomography (ERT), the discretization included 0.05-m thick cells for the shallowest 0.2m, and further 0.1-m thick cells until 0.8-m depth, 0.25-m thick cells until 5-m depth, and 0.5-m thick cells below. The horizontal discretization is 0.25m (half the electrode spacing). The modeling grid was defined to be much larger than the region of interest to ensure reliable inversions. Minimal smoothing was applied. Inversion of only the measurements collected when the distance between the closest injection and potential electrode was equal to or smaller than four times the distance between the injection electrodes gave a lower error of 8% but revealed very identical shallow variations; this indicates that the highest source of error is associated with the imaging of deepest structures. No corrections for temperature dependency were made, although it is recognized that correcting resistivity to a reference temperature of 20°C would lead to lower resistivity values than the values considered here (e.g., Hayley et al. 2007).

Electromagnetic (EM) data

Controlled source inductive EM methods consist of injecting a time- or frequency-varying current in a transmitter coil to create a primary EM field that travels to a receiver coil via paths above and below surface. Governed by Maxwell's equations, the created EM field induces eddy currents in any conductors, which creates a secondary magnetic field. Attributes of this secondary magnetic field, such as amplitude, orientation, and/or phase shift, can be measured by a receiver coil. By isolating these attributes from those of the primary field signal, information about the subsurface electrical conductivity distribution can be inferred (e.g., McNeill 1990; Telford et al. 1990). A review of EM methods for shallow subsurface investigations is given by Everett and Meju (2005).

A frequency domain EM method that is used in this study for shallow subsurface investigations is the EM38 (e.g., McNeill 1980; Geonics 2009), which is a ground conductivity meter that operates at a frequency of 14,500Hz using transmitter receiver coils oriented vertically or horizontally and with an offset distance of 1 and 0.5m. Because this method does not require contact with the ground, data can be acquired very quickly. EM38 data are often displayed as maps of apparent electrical conductivity to highlight lateral variation over large area over an averaged depth interval. More, using different frequency and orientation EM datasets collected over the same region, the data can also be inverted to obtain a model of electrical conductivity (and magnetic susceptibility) distribution that best reproduce the data. Several inversion approaches have been successfully developed for EM measurements (e.g., Farquharson 2000; Triantafilis and Santos 2010; Minsley et al. 2012a).

When the EM38-MK2 system is used (as described in the previous section LiDAR and geophysical datasets and analysis) in the vertical mode with 1-m coil spacing, the signal is expected to be most sensitive to variations at 0.4m below ground surface; variations below 0.2 but above 2m from ground surface contribute to 75% of the response. When using a horizontal mode with a 1-m separation, the contribution from near-surface material is large and decreases almost monotonically with depth, leading to 75% response contribution from the zone above 1m depth (McNeill 1980). When the coils are separated by 0.5m, the contribution depths described in the preceding are approximately half.

The acquired electromagnetic data were inverted at each location to obtain a 1D-subsurface-resistivity model using the least-squares based algorithm EM1DFM (Farquharson 2000). The parameters used in the EM inversion code enforces a fixed trade-off parameter that controls how the objective function is minimized, and that enforces a layered model to be as close as possible to a starting layered model while fitting the data in a given range of uncertainty. The model was defined with 11 resistivity layers of various thickness (from top to bottom, in m: 0.25, 0.1, 0.1, 0.3, 0.3, 0.3, 0.3, 0.3, 0.3, 0.3, 0.2, infinity) and the starting model was defined with 100Ohm.m for the two top layers, 3,000Ohm.m for the next seven layers and 50Ohm.m for the two deepest layers. These model parameters were defined on prior information gained from the probe-measured base of the active layer and ERT profile. Although the obtained mean absolute difference between the calculated and measured EM data is very small (<2%), the calculated model is only one of several possible solutions.

References

Allison I, Bindoff NL, Bindschadler RA, Cok PM, de Noblet N, England MH, Francis JE, Gruber N, Haywood AM, Karoly DJ, Kaser G, Le Quere C, Lenton TM, Mann ME, McNeill BJ, Pitman AJ, Rahmstorf S, Rignot E, Schellnhuber HJ, Schneider SH, Sherwood SC, Somerville RCJ, Steffen K, Steig EJ, Visbeck M, Weaver AJ (2009) The Copenhagen diagnosis, 2009: updating the world on the latest climate science. The University of New South Wales Climate Change Research Centre (CCRC), Sydney

Annan P (2005) GPR methods for hydrogeological studies. In: Rubin Y, Hubbard SS (eds) Hydrogeophysics. Springer, New York

Archie G (1942) The electrical resistivity log as an aid in determining some reservoir characteristics. Pet Trans AIME 146:54–62

 DOI 10.1007/s10040-012-0939-y

Atekwana E, Slater L (2010) Biogeophysics: a new frontier in earth science research. Rev Geophys 47:RG4004. doi:10.1029/2009RG000285
Binley A, Kemna A (2005) DC resistivity and induced polarization methods. In: Rubin Y, Hubbard SS (eds) Hydrogeophysics. Springer, Heidelberg, pp 129–156
Birchak JR, Gardner CZG, Hipp JE, Victor JM (1974) High dielectric constant microwave probes for sensing soil moisture. Proc IEEE 62(1):93–98
Bradford JH, McNamera JP, Boden W, Gooseff MN (2005) Measuring thaw depth beneath peat-lined arctic streams using ground-penetrating radar. Hydrol Process 19:2689–2699
Brosten TR, Bradford JH, McNamara JP, Zarnetske JP, Gooseff MN, Breck Bowden W (2006) Profiles of temporal thaw depths between two Arctic stream types using ground penetrating radar. Permafr Periglac Process 17:341–355
Brosten TR, Bradford JH, McNamara JP, Gooseff MN, Zarnetske JP, Bowden WB, Johnston ME (2009) Estimating 3D variation in active layer thickness beneath Arctic streams using ground penetrating radar. J Hydrol 373:479–486
Cavalli M, Tarolli P, Marchi L, Dalla Fontana G (2008) The effectiveness of airborne LiDAR data in the recognition of channel bed morphology. Catena 73:249–260
Chapin FS III, McGuire AD, Randerson J, Pielke R Sr, Baldocchi D, Hobbie SE, Roulet N, Eugster W, Kasischke E, Rastetter EB, Zimov SA, Running SW (2000) Arctic and boreal ecosystems of western North America as components of the climate system. Glob Chang Biol 6:211–223
Christensen R (2002) Plane answers to complex questions: the theory of linear models, 3rd edn. Springer, New York
Davis JL, Annan AP (1989) Ground-penetrating radar for high-resolution mapping of soil and rock stratigraphy. Geophys Prospect 37:531–551
DePascale G, Pollard WH, Williams KK (2008) Geophysical mapping of ground ice using a combination of capacitive coupled resistivity and ground penetrating radar, Northwest Territories, Canada. J Geophys Res 113:FO2S90. doi:10.1029/2006JF000585
Engstrom R, Hope A, Kwon H, Stow D, Zamolodchiikov D (2005) Spatial distribution of near surface soil moisture and its relationship to microtopography in the Alaskan Arctic Coastal Plain. Nord Hydrol 36(3):219–234
Everett ME, Meju MA (2005) Near-surface controlled source electromagnetic induction: background and recent advances. In: Rubin Y, Hubbard S (eds) Hydrogeophysics, chap 6. Springer, Dordrecht, The Netherlands
Farquharson CG (2000) EM1DFM, University of British Columbia Geophysical Inversion Facility, Vancouver, BC
Fraley C, Raftery A (2012) MCLUST version 4 for R: normal mixture modeling for model-based clustering, classification and density estimation. Technical report no. 597, Department of Statistics, University of Washington, Seatlle, WA
Frankel KL, Dolan JF (2007) Characterizing arid region alluvial fan surface roughness with airborne laser swath mapping digital topographic data. J Geophys Res 112:F02025. doi:10.1029/2006JF000644
Friedlingstein P, Coauthors (2006) Climate–carbon cycle feedback analysis: results from the C4MIP model Intercomparison. J Clim 19:3337–3353
Gangodagamage C, Belmont P, Foufoula-Georgiou E (2011) Revisiting scaling laws in river basins: new considerations across hillslope and fluvial regimes. Water Resour Res 47: W07508. doi:10.1029/2010WR009252
Geonics (2009) EM38-MK2 ground conductivity meter operating manual. Geonics, Mississauga, ON, 42 pp
Glenn NF, Streutker DR, Chadwick DJ, Tahckray GD, Dorsch SJ (2006) Analysis of LIDAR-derived topography information for characterizing and differentiating landslide morphology and activity. Geomorphology 73:131–148
Goswami S, Gamon JA, Tweedie CE (2011) Surface hydrology of an arctic ecosystem: multiscale analysis of flooding and draining experiment using spectral reflectance. J Geophys Res 116: G00I07. doi:10.1029/2010JG001346
Guenther T, Ruecker C, Spitzer K (2006) Three-dimensional modelling and inversion of dc resistivity data incorporating topography: II, inversion. Geophys J Int 166(2):506–517
Harada K, Wada K, Fukuda M (2000) Permafrost mapping by transient electromagnetic method. Permafr Periglac Process 11:71–84
Hastie T, Tibshirani R, Friedman JH (2001) The elements of statistical learning: data mining, inference, and prediction. Springer, New York
Hauck C, Kneisel C (2008) Applied geophysics in periglacial environments. Cambridge University Press, Cambridge
Hauck C, Bottcher M, Maurer H (2010) A new model for quantifying subsurface ice content based on geophysical datasets. Cryosphere Discuss 4:787–821
Hayley K, Bentley LR, Gharibi M, Nightingale M (2007) Low temperature dependence of electrical resistivity: implications for near surface geophysical monitoring. Geophys Res Lett 34(18)
Hilbich C (2010) Time-lapse refraction seismic tomography for the detection of ground ice degradation. Cryosphere 4:243–259
Hilbich C, Hauck C, Hoelzle M, Scherler M, Schudel L, Volksch I, Vonder Muhll D, Mausbacher R (2008) Monitoring mountain permafrost evolution using electrical resistivity tomography: a 7year study of seasonal, annual, and long-term variations at Schilthorn, Swiss Alps. J Geophys Res 113:F01S90. doi:10.1029/2007JF000799
Hinkel KM, Paetzold F, Nelson FE, Bockheim JG (2001a) Patterns of soil temperature and moisture in the active layer and upper permafrost at Barrow, Alaska: 1993–1999. Glob Planet Chang 29:293–309
Hinkel KM, Doolittle J, Bockheim JG, Nelson FE, Paetzold R, Kimble JM, Travis R (2001b) Detection of subsurface permafrost features with ground-penetrating radar, Barrow, Alaska. Permafr Periglac Process 12:179–190
Hinkel KM, Jones BM, Eisner WR, CuomoCJ, Beck RA, Frohn R (2007) Methods to assess natural and anthropogenic thaw lake drainage on the western Arctic coastal plain of northern Alaska. J Geophys Res 112:F02S16, doi:10.1029/2006JF000584
Hubbard S, Linde N (2011) Hydrogeophysics, chap 14. In: Wilderer P (ed) Treatise on water science, vol 1. Academic, Oxford, pp 401–434
Hubbard S, Rubin Y (2005) Hydrogeophysics. In: Rubin Y, Hubbard S (ed) Hydrogeophysics, Springer, Dordrecht, The Netherlands
Jansson JK, Tas N, Brodie EL, Graham DE, Kneafsey TJ, Torn MS, Wu Y, Wullschleger SD, Hubbard SS (2012) Horizontal and vertical profiling of microbial communities across landscape features at NGEE site, Barrow, AK. Fall AGU Meeting Abstract C31C-06, San Francisco, CA
Jorgenson MT, Osterkamp TE (2005) Response of boreal ecosystems to varying modes of permafrost degradation. Can J For Res 35(9):2100–2111. doi:10.1139/x05-153
Jorgenson MT, Shur YL, Pullman ER (2006) Abrupt increase in permafrost degradation in Arctic Alaska. Geophys Res Lett 33: L02503. doi:10.1029/2005GL024960
Kemna A (2000) Tomographic inversion of complex resistivity: theory and application. PhD Thesis, Bochum Ruhr University, Germany
Klute A (1986) Methods of soil analysis, part 1: physical and mineralogical methods. Soil Science Society of America, Madison, WI, pp 399–404
Kneisel C, Hauck C, Fortier R, Moorman B (2008) Advances in geophysical investigations for permafrost investigations. Permafr Periglac Process 19:157–178
Kögel-Knabner I, Amelung W, Cao Z, Fiedler S, Frenzel P, Jahn R, Kalbitz K, Koelbl A, Schloter M (2010) Biogeochemistry of paddy soils. Geoderma 157:1–14. doi:10.1016/j.geoderma.2010
Lashermes B, Foufoula-Georgiou E, Dietrich W (2007) Channel network extraction from high resolution topography using wavelets. Geophys Res Lett 34:L23S04. doi:10.1029/2007GL031140
Lee H, Schuur EAG, Vogel JG (2010) Soil CO_2 production in upland tundra where permafrost is thawing. J Geophys Res 115: G01009. doi:10.1029/2008JG000906
Lee H, Schuur EAG, Vogel JG, Lavoie M, Bhadra D, Staudhammers CL (2011) A spatially explicit analysis to extrapolate carbon fluxes in upland tundra where permafrost is thawing. Glob Chang Biol 17:1379–1393

Leffingwell E (1915) Ground-ice wedges: the dominant form of ground-ice on the north coast of Alaska. J Geol 23:635–654
Liljedahl, AK, Hinzman LD, Schulla J (2012) Ice-wedge polygon type controls low-gradient watershed-scale hydrology. Tenth International Conference on Permafrost, Salekhard, Russia, June 25–29, 2012
Lipson DA, Zona D, Raab TK, Bozzolo F, Mauritz M, Oechel WC (2012) Water-table height and microtopography control biogeochemical cycling in an Arctic coastal tundra ecosystem. Biogeosciences 9:577–591
McKean J, Roering JJ (2004) Landslide detection and surface morphology mapping with airborne laser altimetry. Geomorphology 57:331–351. doi:10.1016/S0169-555X(03)00164-8
McNeill JD (1980) Electromagnetic terrain conductivity measurement at low induction numbers, Technical note TN-6. Geonics, Mississauga, ON, 15 pp
McNeill JD (1990) Use of electromagnetic methods for groundwater studies. In: Ward S (ed) Geotechnical and environmental geophysics, vol 1, Society of Exploration Geophysicists, Tulsa, OK, pp 191–218
Minsley BJ, Smith BD, Hammack R, Sams JI, Veloski G (2012a) Calibration and filtering strategies for frequency domain electromagnetic data. J Appl Geophys 80:56–66
Minsley BJ, Abraham JD, Smith BD, Cannia JC, Voss CI, Jorgenson T, Walvoord MA, Wylie BK, Anderson L, Ball LB, Deszcz-Pan M, Wellman TP, Ager TA (2012b) Airborne electromagnetic imaging of discontinuous permafrost. Geophys Res Lett 39:L02503. doi:10.1029/2011GL050079
Monroe JS, Doolittle JA, Kanevskiy MZ, Hinkle KM, Nelson FE, Jones BM, Shur Y, Kimble JM (2007) Application of ground penetrating radar imagery for three-dimensional visualization of near-surface structures in ice-rich permafrost, Barrow, Alaska. Permafr Periglac Process 18:309–321
Nelson FE, Anisimov OE, Shiklomonov OI (2001) Subsidence risk from thawing permafrost. Nature 410:889–890
Ramirez AL, Nitao JJ, Hanley WG, Aines R, Glaser RE, Sengupta SK, Dyer KM, Hickling TL, Daily WD (2005) Stochastic inversion of electrical resistivity changes using a Markov Chain Monte Carlo approach. J Geophys Res Solid Earth 110(B2): B02101
R Development Core Team (2010) R: A language and environment for statistical computing. R Foundation for Statistical Computing,Vienna, Austria. http://www.R-project.org. November 2012
Revil A, Glover PWJ (1998) Nature of surface electrical conductivity in natural sands, sandstones, and clays. Geophys Res Lett 25(5):691–694
Rowland JC, Jones CE, Altmann G, Bryan R, Crosby BT, Geerneart LG, Hinzman LD, Kane DL, Lawrence DM, Mancino A, Marsh P, McNamara JP, Romanovsky UV, Toniolo H, Travis BJ, Trochim E, Wilson CJ (2010) Arctic landscapes in transition: responses to thawing permafrost. EOS Trans Am Geophys Union 91(26):229–230
Rowland JC, Gangodagamage C, Wilson CJ, Prancevic JP, Brumby SP, Marsh P, Crosby BT (2011), Scaling laws in Arctic permafrost river basins: statistical signature in transition. American Geophysical Union, Washington, DC, Abstract C41C-0424
Scheibe T, Fang Y, Murray CJ, Roden E, Chen J, Chien Y, Brooks S, Hubbard SS (2006) Transport and biogeochemical reactions of metals in a chemically heterogeneous aquifer. Geosphere 2 (4):220–235
Schuur EAG, Vogel JG, Crummer KG, Lee H, Sickman JO, Osterkamp TE (2009) The effect of permafrost thaw on old carbon release and net carbon exchange from tundra. Nature 459:556–559. doi:10.1038/nature08031
Sellmann PV, Brown J, Lewellen RI, McKim H, Merry C (1975) The classification and geomorphic implication of thaw lakes on the Arctic Coastal Plain, Alaska. Research report 344, US Army CRREL, Hanover, NH
Shiklomanov NI, Streletskiy DA, Nelson FE, Hollister RD, Romanovsky VE, Tweedie CE, Bockheim JG, Brown J (2010) Decadal variations of active-layer thickness in moisture-controlled landscapes, Barrow, Alaska. J Geophys Res 115:G00I04
Sommerkorn M (2008) Micro-topographic patterns unravel controls of soil water and temperature on soil respiration in three Siberian tundra systems. Soil Biol Biogeochem 40:1792–1802. doi:10.1016/j.soilbio.2008.03.002
Steelman CM, Endres AL (2009) Evolution of high-frequency ground-penetrating radar direct ground wave propagation during thin frozen soil layer development. Cold Reg Sci Technol 57:116–122
Steelman CM, Endres AL, van der Kruk J (2010) Field observations of shallow freeze and thaw processes using high frequency ground penetrating radar. Hydrol Process 24:2022–2033
Sturm M, Racine CR, Tape K (2001) Increasing shrub abundance in the Arctic. Nature 411:546–547
Sturtevant CS, Oechel WC, Zona D, Kim Y, Emerson CE (2012) Soil moisture control over autumn season methane flux, Arctic Coastal Plain of Alaska. Biogeosciences 9:1423–1440
Tarnocai C, Canadell JG, Schuur EAG, Kuhry P, Mazhitova G, Zimo S (2009) Soil organic carbon pools in the northern circumpolar permafrost region. Global Biogeochem Cycles 23: GB2023
Telford WM, Geldart LP, Sheriff RE (1990) Applied geophysics. Cambridge University Press, Cambridge, 792 pp
Topp GC, Davis JL, Annan AP (1980) Electromagnetic determination of soil water content: measurement in coaxial transmission lines. Water Resour Res 16:579–582
Triantafilis J, Santos FAM (2010) Resolving the spatial distribution of the true electrical conductivity with depth using EM38 and EM31 signal data and a laterally constrained inversion model. Aust J Soil Res 48(5):434–446
Wainwright H, Hubbard SS, Gangodagamage C. Dafflon B, Ulrich C, Wu Y, Wilson C, Tweedie C, Wullschleger S (2012) Multiscale Bayesian Fusion approach using geophysical and remote sensing data for characterizing arctic tundra hydrogeochemical properties, Tenth Int. Conf. on Permafrost, Salekhard, Russia, June 25–29
Watanabe K, Wake T (2009) Measurements of unfrozen water content and relative permittivity of frozen unsaturated soil using NMR and TDR. Cold Reg Sci Technol 59:34–41
Westermann S, Wollschläger U, Boike J (2010) Monitoring of active layer dynamics at a permafrost site on Svalbard using multi-channel ground-penetrating radar. Cryosphere 4:475–487. doi:10.5194/tc-4-475-2010
Wollschläger U, Gerhards H, Yu Q, Roth K (2010) Multi-channel ground-penetrating radar to explore spatial variations in thaw depth and moisture content in the active layer of a permafrost site. Cryosphere 4:269–283. doi:10.5194/tc-4-269-2010
Woo MK, Guan XJ (2006) Hydrological connectivity and seasonal storage change of tundra ponds in a polar oasis environment: Canadian High Arctic. Permafr Periglac Process 17:309–323
Wright N, Hayashi M, Quinton WL (2009) Spatial and temporal variations in active layer thawing and their implications on runoff generation in peat-covered permafrost terrain. Water Resour Res 45:W05414
Wu Y, Ajo-Franklin J, Spycher N, Hubbard SS, Zhang G, Williams KH, Taylor J, Fujita Y, Smith R (2011) Geophysical monitoring and reactive transport modeling of ureolytically-driven calcium carbonate precipitation. Geochem Trans 12(7): doi:10.1186/1467-4866-12-7
Wu Y, Hubbard SS, Ulrich C, Wullshleger S (2012) Remote monitoring of freeze-thaw transitions in Arctic soils using the complex resistivity method. Vadose Zone J. doi:10.2136/vzj2012.0062
Yoshikawa K, Leuschen, C, Ikeda A, Harada K, Gogineni P, Hoekstra P, Hinzman L, Sawada Y, Matsuoka N (2006) Comparison of geophysical investigations for detection of massive ground ice (pingo ice). J Geophys Res 111:E06S19
Zimov SA, Schuur EAG, Chapin FS (2006) Permafrost and the global carbon budget. Science 312:1612–1613
Zona D, Lipson DA, Zulueta RC, Oberbauer SF, Oechel WC (2011) Microtopographic controls on ecosystem functioning in the Arctic Coastal Plain. J Geophys Res 116:G00I08. doi:10.1029/2009JG0011214